Supplementary Information

From Precursor to Performance: The Impact of FAI Impurities on Halide Perovskite Thin Films and Devices

Siyu Yan,[a] *Saqlain Choudhary,* [a] *Emily A. Hudson,*[a] *Ruohan Zhao,*[a] *Henry J. Snaith,*[a] *Michael B. Johnston*[a] *and Nakita K. Noel**[a]

[a] Department of Physics, University of Oxford, Clarendon Laboratory, Parks Road, OX1 3PU, UK

E-mail: nakita.noel@physics.ox.ac.uk

Table of Contents

Experimental Section

1. Materials and Chemicals

For spin-coated perovskite films, lead iodide (PbI_2, 99.99%) was purchased from TCl Chemicals. Cesium iodide (CsI, 99.99%) and lead bromide ($PbBr_2$, >98%) were purchased from Alfa Aesar. Formamidinium iodide (FAI) was purchased from Greatcell Solar and Dyenamo. For vapour-deposited perovskite, PbI_2 (99.999%, metal basis) was purchased from Alfa-Aesar. Formamidinium iodide (FAI) purchased from Greatcell Solar (supplier A) with different batch numbers (batch 1: 485105; batch 2: 508004), was used as as-received FAI. Recrystallised FAI was obtained by the recrystallisation of as-received FAI as detailed below. High-purity FAI was purchased from Dyenamo (supplier B), batch number N6Q1X. Fullerene (C60, 99.9%) was purchased from Acros Organics. Tin (IV) oxide (SnO_2, 15% in H_2O colloidal dispersion) was purchased from Alfa Aesar. Poly[bis(4-phenyl)(2,4,6-trimethylphenyl)amine (PTAA) was purchased from Xi'an Polymer Light Technology. [4-(3,6-Dimethyl-9H-carbazol-9-yl)butyl]phosphonic acid (Me-4PACz, >99.0%) was purchased from TCI. Unless stated otherwise, all other materials and solvents were purchased from Sigma-Aldrich. In this work, apart from recrystallised FAI, all materials were used as received without further purification.

Recrystallised FAI precursor

Greatcell FAI powder was dissolved in ethanol heated at 75°C to obtain a supersaturated solution. Once the FAI was fully dissolved, the solution was removed from the hotplate and was left to naturally cool to room temperature. After approximately one hour, the mixture was placed in a freezer at 5°C overnight. Large crystals of FAI were then harvested from the mother liquor through vacuum filtration. The FAI crystals were washed with diethyl ether three times and subsequently dried in a vacuum oven at 40°C for two days. After cooling down to room temperature, the recrystallised FAI was stored in a nitrogen-filled glovebox. Before evaporation, the recrystallised FAI was ground into a fine powder, ensuring a grain size and packing density comparable to those of the as-received material.

2. Perovskite and Film Fabrication

Substrate Cleaning

Indium-doped tin oxide (ITO) coated glass (Biotain, 30 x 30 x 1.1 mm, 10~15 ohm/sq) substrates were cleaned in a series of ultrasonic baths using industrial detergent Decon90 (1% vol in deionized water), deionized water, acetone, and isopropyl alcohol (each step for 5 minutes). After ultrasonic cleaning, the substrates were dried with nitrogen gas, and the substrates were then placed in the UV-Ozone for 15 minutes.

Hole Transport Layers

PTAA was dissolved in toluene at a concentration of 2 mg/mL. 100 μL solution was dynamically deposited onto a substrate at 6000 rpm for 30 s. After spin-coating, the substrate was annealed at 100 ºC for 10 minutes. The substrate was then removed from the hotplate and allowed to cool down to room temperature, after which it was ready for the deposition of subsequent layers.

Me-4PACz was dissolved in ethanol at a concentration of 0.33 mg/mL. 350 μL solution was statically deposited onto a substrate and allowed to spread for 10 s. The substrate was then subjected to spin-coating at 3000 rpm for 30 s. After spin-coating, the substrate was annealed at 100 ºC for 10 minutes. After cooling down to room temperature, Al_2O_3 nanoparticles (1:150 vol% in 2-propanol) were spin coated dynamically on top of the Me-4PACz at 2000 rpm for 20 seconds as a wetting agent. The film was annealed at 100 ºC for 1min. After cooling down to room temperature, the substrate was ready to use.

Electron Transport Layers

25 nm of C_{60} was vacuum-deposited at 0.1 Å/s in a thermal evaporator. 5 nm BCP was then deposited on top of the C_{60} at an evaporation rate of 0.1 Å/s.

200 μL SnO_2 colloidal solution (diluted to 2.5 weight % in deionized water) was deposited by static spin-coating at 3000 rpm for 30 s (1000 rpm ramp), followed by annealing at 150°C for 30 min in ambient air.

Perovskite Thin Films

For spin-coated perovskite films, PbI_2, $PbBr_2$, FAI, CsI were weighed stoichiometrically in a N_2-filled glovebox to the target composition ($FA_{0.83}Cs_{0.17}Pb(I_{0.8}Br_{0.2})_3$). The precursor salts were dissolved in a mixture (4:1 ratio by volume) of dimethylformamide (DMF) and dimethylsulfoxide (DMSO) to obtain a perovskite concentration of 1.3 M. The precursor solution was left stirring at room temperature overnight in a glovebox before use. To deposit the perovskite layer, the perovskite precursor ink (175 μL) was dispensed dynamically onto a substrate spinning at 1000 rpm. The substrate was accelerated to 5000 rpm over the course of 5 seconds and remained at this speed for 35 seconds. 5 seconds before the end of the process, anisole (335 μL) was applied to the spinning substrate as an anti-solvent quench. The films were then annealed at 100 °C for 60 minutes in a N_2-filled glovebox. After cooling down to room temperature, films were ready to use.

For vapour-deposited perovskite films, FAI, PbI_2 were co-evaporated with the molar ratio of FAI: PbI_2 = 1: 1 in a custom-built thermal evaporator chamber using an in situ residual gas analysis (RGA) system to deposit 600 nm films with a final composition of $FAPbI_3$ (Given that the optimised FAI equivalent rate is related to the type of substrate, in this work, all co-evaporated $FAPbI_3$ films were deposited on 3nm PbI_2/substrate to effectively decouple the crystallisation of perovskite from the influence of substrate materials. Under this condition, the optimised equivalent ratio of FAI/PbI_2 was determined to be 1/1.). During the evaporation, the pressure was typically $< 1 \times 10^{-5}$ mbar. The source rates were kept constant using gold-plated quartz crystal microbalances (QCM) and PID-loop-control software. The sublimation rate of the FAI was controlled using QCMs adjacent to the crucible. Unless otherwise specified, all vapour-deposited perovskite samples were annealed in an N_2 glovebox at 150 °C for 5 minutes followed by 25 minutes at 135 °C. After cooling down to room temperature, films were ready to use.

Electrodes

100 nm silver (Ag) or 80 nm gold (Au) contacts were thermally evaporated with shadow masks under high vacuum ($< 6 \times 10^{-6}$ torr) using a thermal evaporator (Nano 36, Kurt J. Lesker).

3. Details of RGA system

The composition of the residual gas in the thermal evaporator chamber during the deposition was monitored using a residual gas analyser (RGA, Hiden Analytical Limited). The RGA system consists of an RC Interface Unit (IU), a Radio Frequency (RF) Head, and a Probe installed directly within the vacuum system. The Probe comprises a quadrupole mass analyser equipped with an electron-impact ion source for ionisation of neutral particles, and a detector for measuring the mass-resolved ion current. Data acquisition was performed using the MASsoft Windows-based software. Before turning on the in situ RGA system, the evaporator chamber was pumped down to a base pressure below 5×10^{-6} mbar. For all measurements conducted in this work, the Faraday detector was used over a mass range up to 300 amu. The minimum detectable partial pressure of the Faraday detector is approximately 1×10^{-11} mbar.

4. X-ray Diffraction Measurements

X-ray diffraction measurements (XRD) were taken using a Panalytical X-pert powder diffractometer. The Cu-Kα X-ray source (λ=1.54 Å) was set to 40 kV voltage and 40 mA current. The XRD patterns were corrected by shifting the 2θ-axis based on the ITO substrate reference peak at $2\theta=30.3^{\circ}$ or the z-cut quartz substrate reference peak at $2\theta=16.433^{\circ}$.[1]

5. Nuclear Magnetic Resonance (NMR) Spectroscopy

A two-channel Bruker Avance III HD Nanobay 400 MHz instrument running TOPSPIN 3 equipped with a 5 mm z-gradient broadband/fluorine observation probe is used to measure ^{1}H proton NMR spectroscopy. The signal from deuterated DMF or deuterated DMSO solvent is used for reference.

6. Absorption Spectra

Fourier Transform Infrared Measurements

Absorption spectra were carried out using a Bruker Vertex 80v Fourier-Transform Infrared (FTIR) spectrometer with a near-infrared source, calcium fluoride beam splitter and a silicon diode detector. ITO or quartz substrates were used as reference substrates here. The absorption coefficient (α) was calculated using the following formula

$$\alpha = \frac{1}{d} log_{10}\left(\frac{1 - R}{T}\right), \qquad \text{(Eq-S1)}$$

where R is the reflectance spectrum, T is the transmittance spectrum, and d is the film thickness.

Elliott Fitting

The absorption coefficient spectra were fitted by the Elliott's model to obtain the optical bandgap (E_g), exciton binding energy (E_b) and electronic sub-bandgap disorder (Υ). The Elliott's model represents the total absorption coefficient ($\alpha(E)$) as a linear combination of the absorption coefficient from bound excitons ($\alpha_X(E)$) and electron-hole continuum states ($\alpha_C(E)$) for a direct semiconductor as shown below[1, 2]

$$\alpha(E) = \alpha_X(E) + \alpha_C(E), \qquad \text{(Eq-S2)}$$

The contribution from $\alpha_X(E)$ is expressed as

$$\alpha_X(E) = \frac{b_0}{E} \sum_{n=1}^{\infty} \frac{4\pi E_b^{3/2}}{n^3} \delta\left(E - \left[E_g - \frac{E_b}{n^2}\right]\right), \qquad \text{(Eq-S3)}$$

where b_0 is a constant of proportionality that includes the electric dipole transition matrix element between the valence and conduction band, $|\langle \Psi_c | P | \Psi_v \rangle|^2$ and n is a positive integer quantum number. Eq-S3 describes a lines series at energies $-E_b/n^2$ below E_g and their magnitudes are proportional to $-1/n^3$. The contribution from $\alpha_C(E)$ is expressed as

$$\alpha_C(E) = \frac{b_0}{E}\left[\frac{2\pi\sqrt{\frac{E_b}{E-E_g}}}{1-exp\left(-2\pi\sqrt{\frac{E_b}{E-E_g}}\right)}\right]c_0^{-1}JDoS(E) \quad , \qquad \text{(Eq-S4)}$$

where the joint density of states ($JDoS$) is given by

$$JDoS(E) = \begin{cases} c_0\sqrt{E-E_g}, & for\ E > E_g \\ 0, & otherwise \end{cases}, \qquad \text{(Eq-S5)}$$

and the joint density of states constant (c_0) is given by

$$c_0 = \frac{1}{(2\pi)^2}\left(\frac{2\mu}{\hbar^2}\right)^{3/2} \times 2 \quad , \qquad \text{(Eq-S6)}$$

where μ is the reduced effective mass of the electron-hole system, which is assumed to be 0.15 m_e.[3] The term in the square brackets in Eq-S4 is the Coulombic enhancement factor (ξ), which represents the probability of an electron and a hole existing in the same space. The second term $c_0^{-1}JDoS(E)$ represents the absorption coefficient of free electrons and holes in the absence of Coulombic attraction, $\alpha_{Free}(E)$.

The linear combination of the contributions from the excitonic and continuum states as shown in Eq-S2 is then convolved with a broadening function, which is written as

$$g(E) = \frac{1}{\cosh\frac{E-E_x}{\gamma}} \quad , \qquad \text{(Eq-S7)}$$

where γ is assigned as the electronic sub-bandgap disorder, $E_x = E_g$ when convolved with $\alpha_C(E)$,and E_x is equal to the line series when convolved with $\alpha_X(E)$. It is worth noting that γ is also attributed to an electron-phonon coupling in other literature but with the absence of temperature dependence measurements, we mainly attribute the broadening to the degree of disorder.[2, 4]

7. Photoluminescence Measurements

Steady-State Photoluminescence Measurements

A 398 nm diode laser (PicoHarp, LDH-D-C-405M) was used to illuminate the samples, on a continuous wave with the intensity of 160 mW/cm^2. The PL emitted by the samples was coupled into a grating spectrometer (Princeton Instruments, SP-2558) and then directed onto a silicon iCCD (PI-MAX4, Princeton Instruments). The samples were measured in nitrogen atmosphere.

Time-Resolved Photoluminescence Measurements

For the TRPL measurement presented in Figure S18b: A TimeHarp300 (Picoquant) system equipped with a PMT detector (dead time < 95 ps) and single-photon counting electronics (TimeHarp260 nano) was used to measure the samples in an air atmosphere. To ensure that we only measure single photons, the pile-up rate (defined as the ratio of rate of emission to the rate of excitation) was kept below 5%.

For all other TRPL measurements: A 398 nm picosecond pulsed diode laser (PicoHarp, LDH-D-C-405M) operated at 2.5MHz, with the fluence of 45.4 nJ/cm^2 was used to measure the samples in nitrogen atmosphere. The PL emitted by the samples was collected by a photon-counting detector (PDM series from MPD) and the timing was controlled using a PicoHarp300 event timer.

8. Device Measurements

Current Density-Voltage Characteristics

The current density-voltage (J-V) characteristics for perovskite solar cells were measured in air using a Keithley 2400 source meter under approximately 100 mW/cm^2 of AM1.5G irradiation generated by an ABET Sun 2000 Class A simulator. Before the device measurement, the intensity of the solar simulator was automatically measured by a KG5 filtered silicon reference cell (certified by Fraunhofer ISE) to calibrate the accurate power conversion efficiency (PCE). The illuminated active area was 0.25 cm^2 defined by black anodised metal masks. The *J-V* curves were taken from 1.2 V to -0.2 V and followed by the forward scan (from -0.2 V to 1.2 V), at a scan rate of 0.33 V/s in each direction.

External Quantum Efficiency

The external quantum efficiency (EQE) of devices was measured using a Fourier transform photocurrent spectrometer in the FTIR setup mentioned in section 5. The active area of the devices (0.25 cm^2) was illuminated by a tungsten halogen lamp. The accurate EQE value was calibrated by a Newport-calibrated reference silicon solar cell of a known EQE.

The integrated current density from the EQE measurement was determined by the overlap integral of the AM1.5 photon flux with the EQE.[5]

Supporting Data and Discussion

1. Impurity Analysis

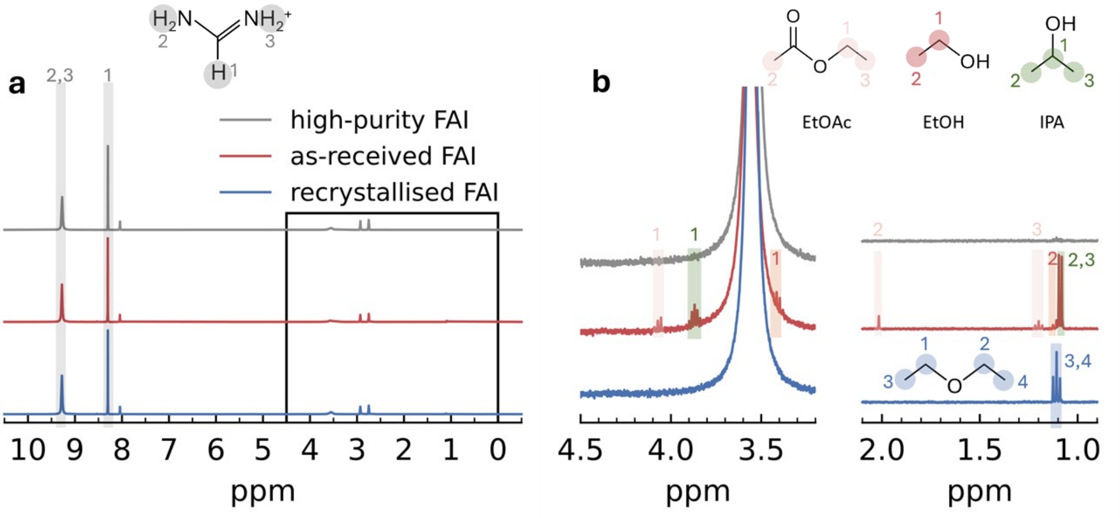

Figure S1 (a) NMR spectroscopy of high-purity FAI, as-received FAI and recrystallised FAI (dissolved in DMF-d_7) across a wide spectral range. The as-received FAI and recrystallised FAI shown here are from a different recrystallisation run than with the results shown in the main text (Figure 1). We note however, that the effect of the recrystallisation is the same. (b) Isolated and magnified areas of interest from spectra in (a) showing signal from the impurities in FAI.

2. Solution-Processed Perovskite Films and Devices

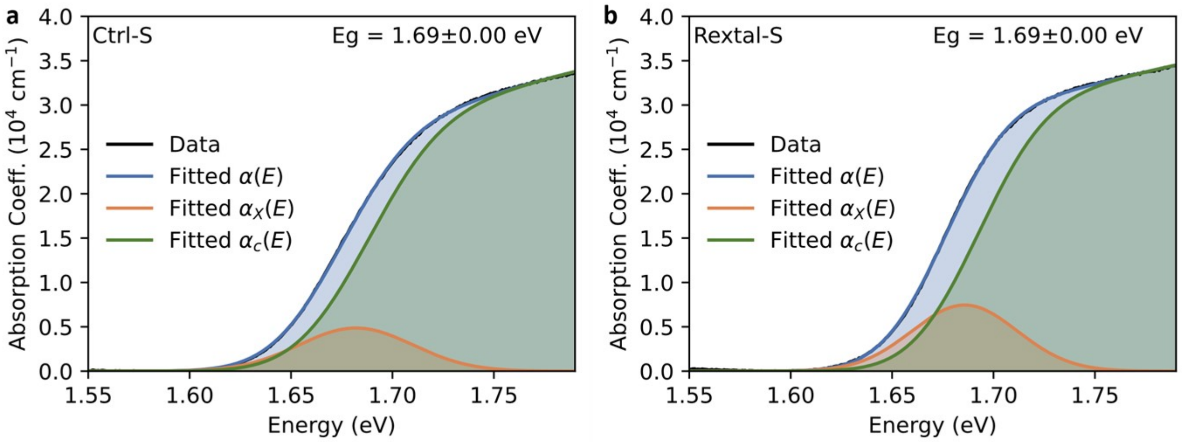

Figure S2 Elliott fitting results of the absorption coefficient values of solution-processed $FA_{0.83}Cs_{0.17}Pb(I_{0.8}Br_{0.2})_3$ MHP films fabricated using as-received and recrystallised FAI, abbreviated as ctrl-S and rextal-S films in the figure, respectively.

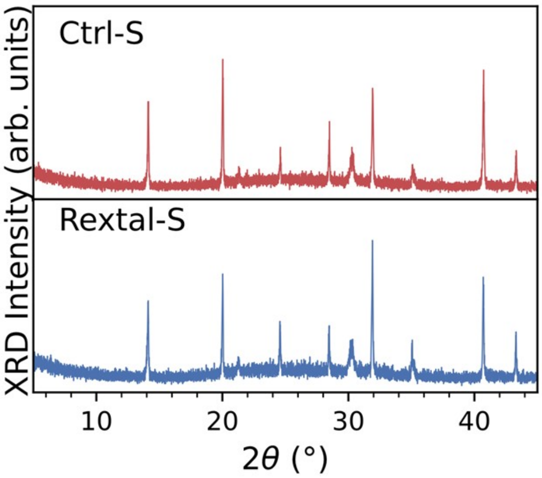

Figure S3 X-ray diffraction patterns of solution-processed $FA_{0.83}Cs_{0.17}Pb(I_{0.8}Br_{0.2})_3$ MHP films made by as-received and recrystallised FAI, abbreviated as ctrl-S and rextal-S films in the figure, respectively.

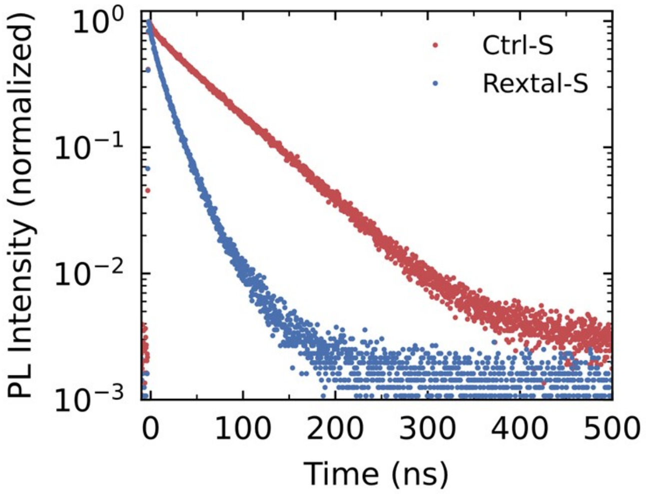

Figure S4 PL dynamics of solution-processed $FA_{0.83}Cs_{0.17}Pb(I_{0.8}Br_{0.2})_3$ MHP films made using as-received FAI and recrystallised FAI, abbreviated as ctrl-S and rextal-S films in the figure, respectively, excited by 398nm-wavelength laser, with the 1MHz repetition rate and the fluence of 45.4 nJ/cm^2.

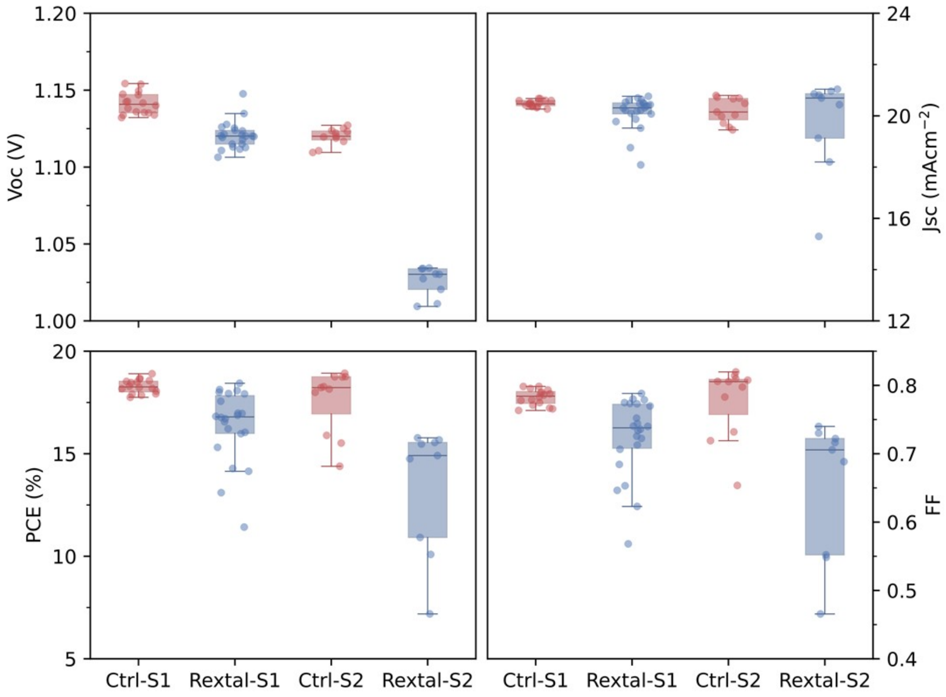

Figure S5 Statistical distribution of photovoltaic performance parameters of solution-processed $FA_{0.83}Cs_{0.17}Pb(I_{0.8}Br_{0.2})_3$ MHP devices made by as-received and recrystallised FAI made in two separate batches (labelled as ctrl-S1, rextal-S1 and ctrl-S2, rextal-S2).

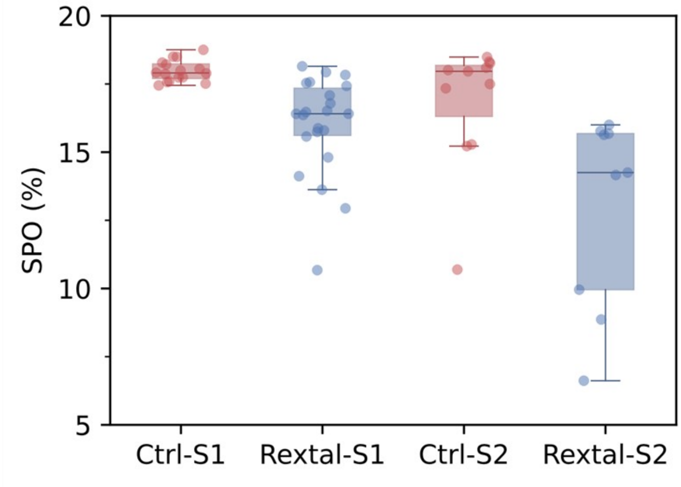

Figure S6 Stabilised power output of solution-processed $FA_{0.83}Cs_{0.17}Pb(I_{0.8}Br_{0.2})_3$ MHP devices with as-received and recrystallised FAI made in two separate batches (labelled as ctrl-S1, rextal-S1 and ctrl-S2, rextal-S2).

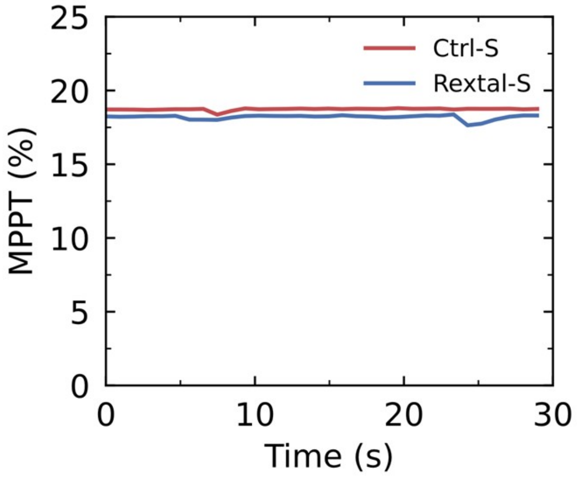

Figure S7 Maximum power output tracking (MPPT) of best solution-processed $FA_{0.83}Cs_{0.17}Pb(I_{0.8}Br_{0.2})_3$ MHP devices made by as-received FAI (ctrl-S) and recrystallised FAI (rextal-S).

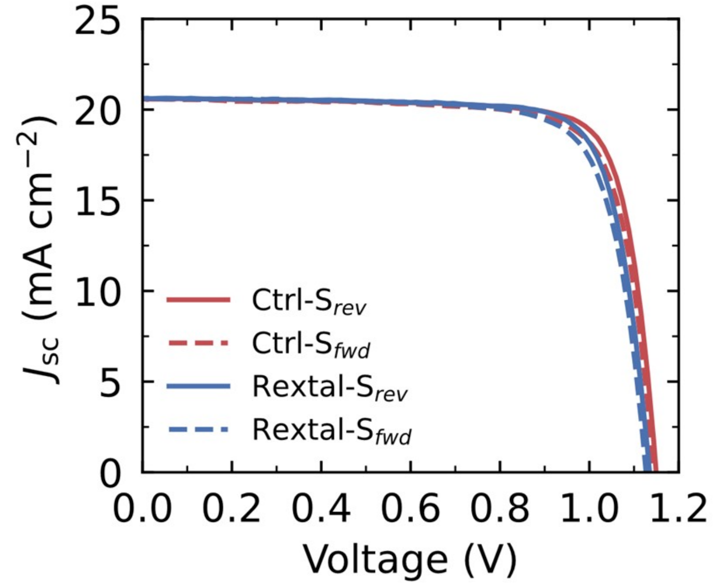

Figure S8 Current density-voltage curve of best solution-processed $FA_{0.83}Cs_{0.17}Pb(I_{0.8}Br_{0.2})_3$ MHP devices made by as-received and recrystallised FAI (labelled as ctrl-S and rextal-S).

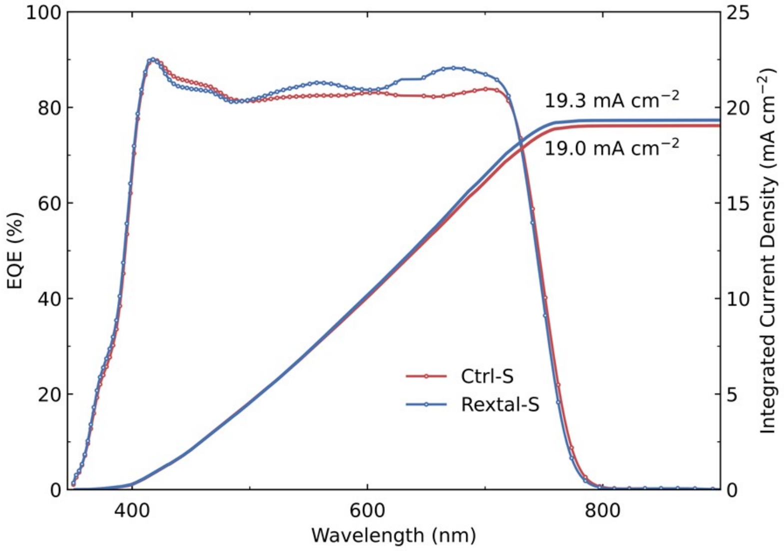

Figure S9 EQE, and integrated current density for the solution-processed $FA_{0.83}Cs_{0.17}Pb(I_{0.8}Br_{0.2})_3$ MHP devices made by as-received and recrystallised FAI (labelled as ctrl-S and rextal-S).

Table S1 Champion and average device performance parameters for solution-processed $FA_{0.83}Cs_{0.17}Pb(I_{0.8}Br_{0.2})_3$ perovskite solar cells fabricated with as-received (ctrl-S) and recrystallised (rextal-S) FAI measured under 1 sun simulated AM1.5G solar illumination. The values given in this table represent scans from open-circuit to short-circuit conditions.

Device		J_{sc}(mA cm^{-2})	V_{oc} (V)	PCE (%)	FF	SPO (%)
Ctrl-S	Champion	20.80	1.13	18.93	0.82	18.50
	Avg	20.48±0.13	1.14±0.01	18.29±0.34	0.78±0.01	17.97±0.39
Rextal-S	Champion	20.62	1.13	18.44	0.79	18.15
	Avg	20.13±0.64	1.12±0.01	16.37±1.78	0.72±0.06	15.98±1.82

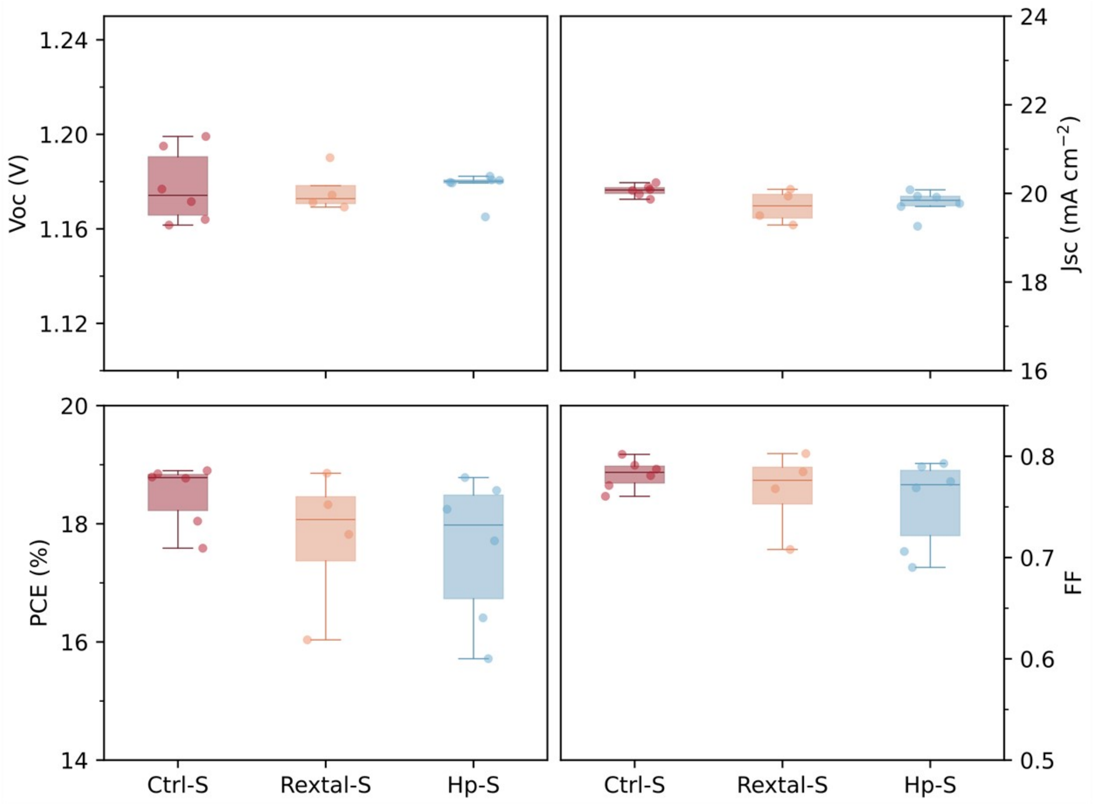

Figure S10 Photovoltaic performance parameters of solution-processed $FA_{0.83}Cs_{0.17}Pb(I_{0.8}Br_{0.2})_3$ MHP devices made by as-received FAI (ctrl-S), recrystallised FAI (rextal-S) and high-purity FAI (hp-S).

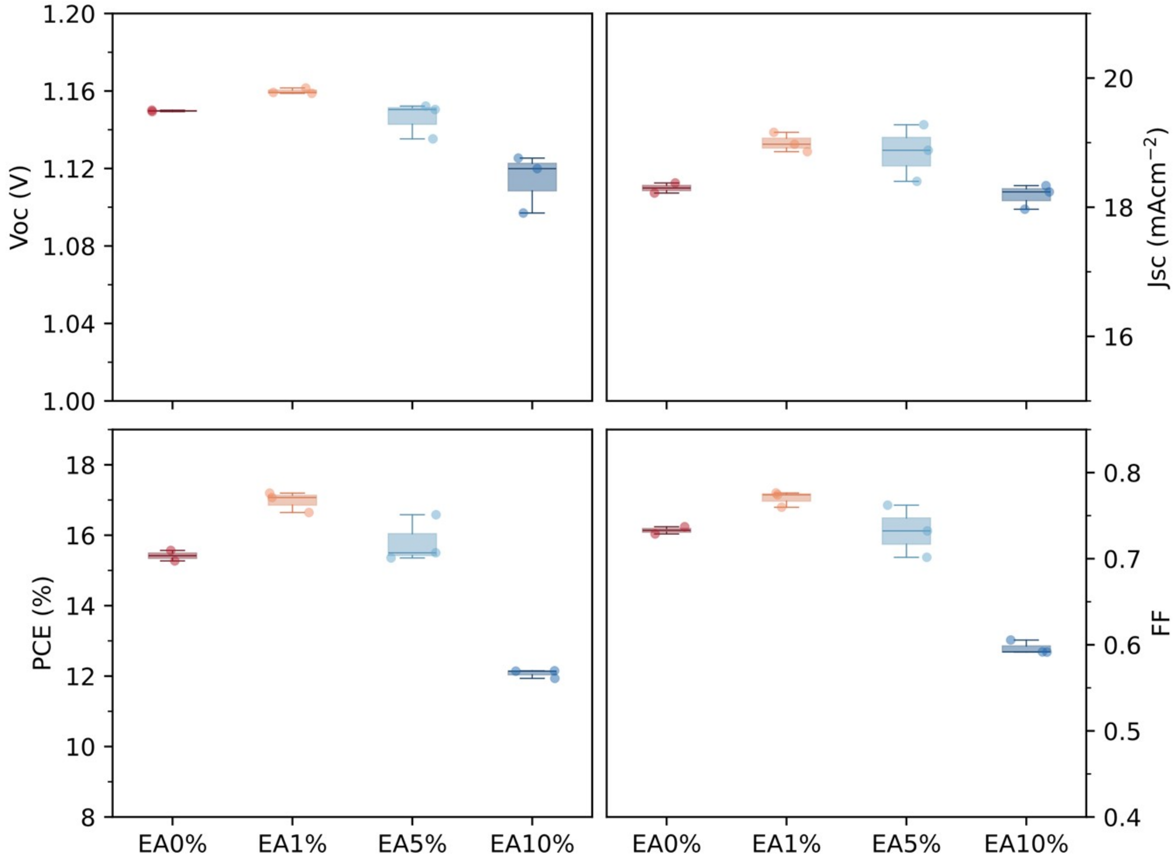

Figure S11 Photovoltaic performance parameters of solution-processed $FA_{0.83}Cs_{0.17}Pb(I_{0.8}Br_{0.2})_3$ MHP devices made by the perovskite precursor using recrystallised FAI with adding different amounts of ethyl acetate (EA 0 vol%, 1 vol%, 5 vol% and 10 vol%).

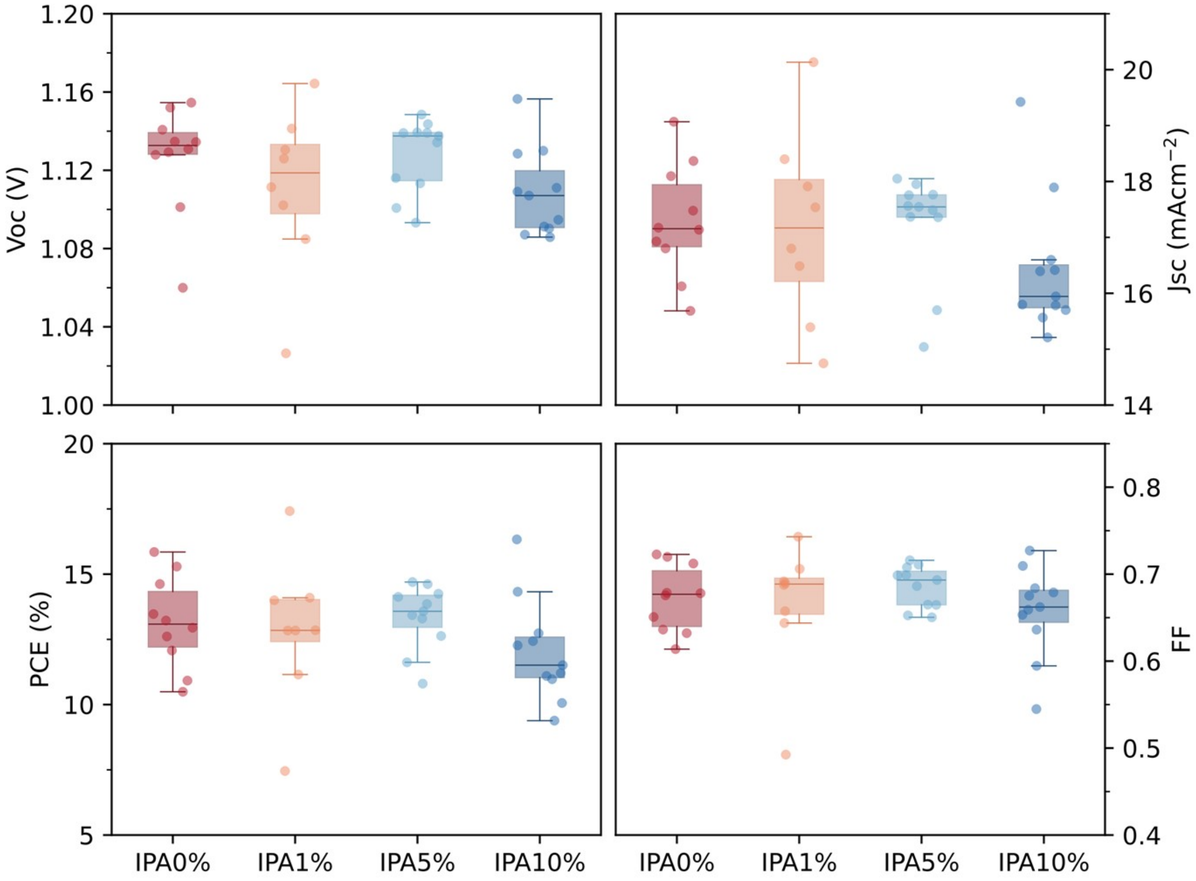

Figure S12 Photovoltaic performance parameters of solution-processed $FA_{0.83}Cs_{0.17}Pb(I_{0.8}Br_{0.2})_3$ MHP devices made by the perovskite precursor using recrystallised FAI with adding different amounts of isopropanol (0 vol%, 1 vol%, 5 vol% and 10 vol%).

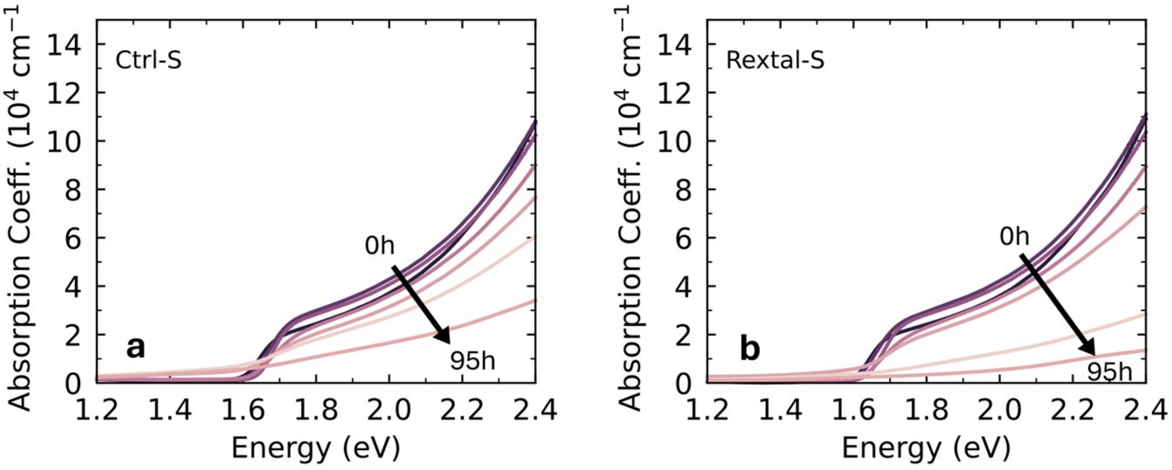

Figure S13 The absorption coefficient spectra of solution-processed $FA_{0.83}Cs_{0.17}Pb(I_{0.8}Br_{0.2})_3$ MHP films made by as-received FAI (ctrl-S) and recrystallised FAI (rextal-S) aged at 70 ± 5°C under 0.76 sun illumination in the ambient atmosphere from 0h to 95h.

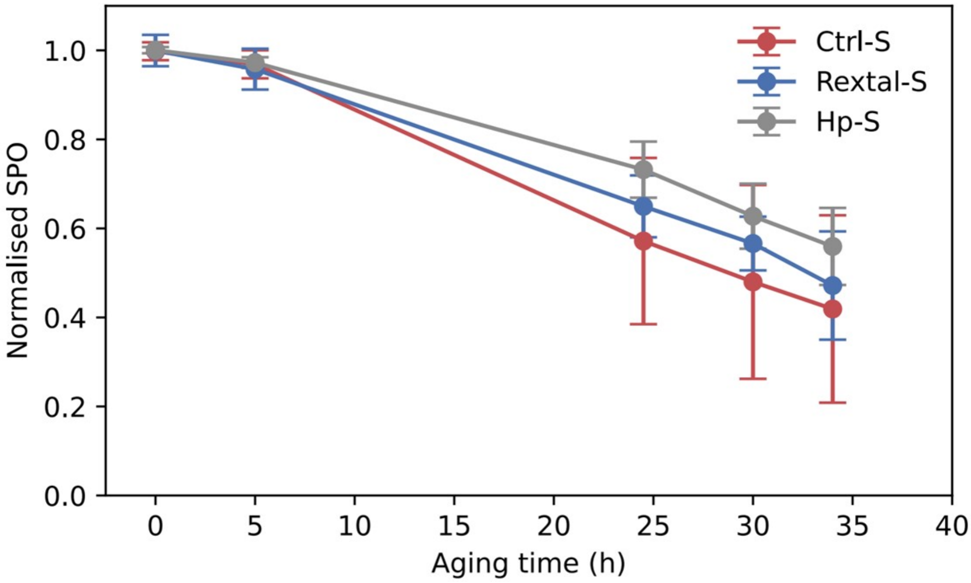

Figure S14 Evolution of normalised stabilised power outputs (SPOs) of unencapsulated cells aged at 70 ± 5°C under 0.76-sun illumination in the ambient atmosphere (four cells for each condition). The absorber layers are solution-processed $FA_{0.83}Cs_{0.17}Pb(I_{0.8}Br_{0.2})_3$ MHP films, made using as-received FAI (labelled as ‘ctrl-S’ in the figure), recrystallised FAI (labelled as ‘rextal-S’ in the figure) and high-purity FAI (labelled as ‘hp-S’ in the figure). The device structure is ITO/SAM/Al_2O_3/spin-coated MHP/C60/Bathocuproine (BCP)/Ag.

3. Vapour-Processed Perovskite Films and Devices

Optimisation Process and Evaporation Parameters

We note that these procedures may require adjustment for different deposition systems due to variations in chamber geometry and working distances; however, the underlying principles remain generally applicable.

Tooling factors for each FAI precursor are determined from independent single-source evaporation experiments by comparing the substrate QCM readings with the film thickness measured ex situ. These tooling factors therefore represent the ratio between the real deposition rate and the substrate QCM reading.

During single-source FAI evaporation for the mass spectrometry measurements, the tooling factors are applied to relate the substrate QCM reading to the corresponding real deposition rate (~0.19 Å s^{-1}), ensuring consistency with actual deposition conditions.

During co-evaporation, the PbI_2 deposition rate is controlled using the source QCM, while the FAI flux is monitored using a substrate-positioned QCM operated with a tooling factor of 1. The tooling factors are then used to determine the appropriate QCM setpoints required to achieve a consistent real FAI deposition rate (~0.19 Å s^{-1}) across all samples.

The overall perovskite growth rate (~0.40 Å s^{-1}) is determined from the film thickness divided by the deposition time and is consistent across all conditions. The corresponding source QCM rates, tooling factors, and deposition parameters for all precursors are summarised in Table S2.

The PbI_2 source temperature is kept consistent across all depositions. Although slight variations in chamber pressure are observed between different FAI precursors, the maximum pressure remains below 1.5×10^{-5} mbar. Under these conditions, the mean free path (~60–100 cm) is significantly larger than the source-to-substrate distance (~30–35 cm), indicating that gas-phase scattering effects are negligible and do not significantly affect the deposition rates or stoichiometry.

Differences in tooling factors between FAI precursors are therefore attributed primarily to variations in evaporation behaviour (e.g., precursor purity and sublimation characteristics), rather than pressure-induced transport effects.

Table S2 Deposition parameters used during co-evaporation of $FAPbI_3$ films using as-received (ctrl-V), recrystallised (rextal-V), and high-purity (hp-V) FAI. Source QCM rates, precursor-specific tooling factors, and corresponding real deposition rates are listed for each condition. The total perovskite growth rate is derived from the measured film thickness and deposition time.

	Ctrl-V	Rextal-V	Hp-V
PbI_2 source QCM rate (Å s^{-1})	0.56	0.56	0.56
PbI_2 real deposition rate (Å s^{-1})	0.20	0.20	0.20
FAI source QCM rate (Å s^{-1})	6.13	5.76	6.32
FAI tooling factor*	0.23	0.18	0.14
FAI real deposition rate (Å s^{-1})	0.19	0.19	0.19
Substrate QCM rate (Å s^{-1})	1.22	1.46	1.76
$FAPbI_3$ real deposition rate (Å s^{-1})	0.40	0.40	0.40
PbI_2 source temperature (°C)	275.10	274.96	273.20
FAI source temperature (°C)	174.36	164.40	169.20
Substrate temperature (°C)	22.00	21.54	21.50
Chamber pressure (mbar)	3.07×10^{-6}	2.97×10^{-6}	1.35×10^{-6}

* Determined from independent single-source evaporation calibration as the ratio between the real deposition rate (from thickness measurements) and the substrate QCM reading.

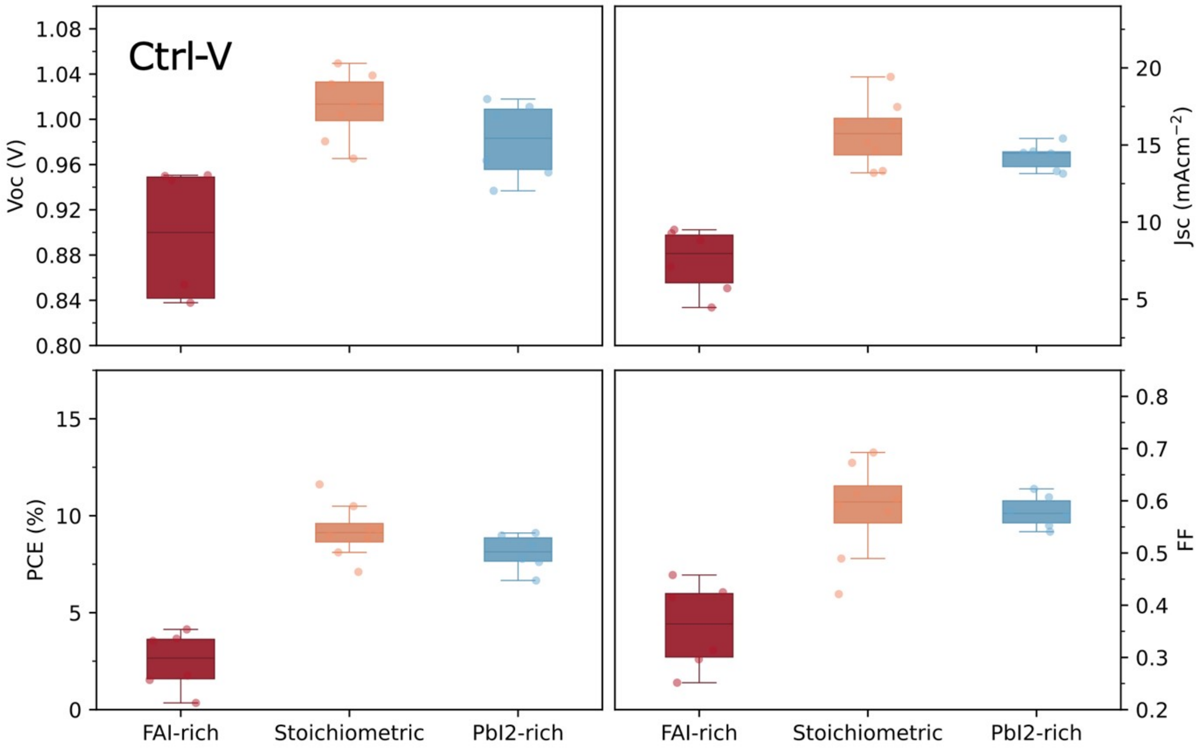

Figure S15 Stoichiometry optimisation for $FAPbI_3$ perovskite devices fabricated with as-received FAI (ctrl-V). Device performance parameters are shown for FAI-rich (FAI +5 mol%), stoichiometric ($FAI:PbI_2$ = 1:1)and PbI_2-rich (PbI_2 + 5mol%) conditions. In the box plots, the central line inside each box represents the median value of the dataset. The box edges (lower and upper sides) indicate the first quartile (Q1) and third quartile (Q3), corresponding to the 25th and 75th percentiles, respectively. The whisker extends from the box to the smallest and largest data points within 1.5 times the interquartile range (IQR) from Q1 and Q3. Data points lying outside of this range are plotted individually as outliers.

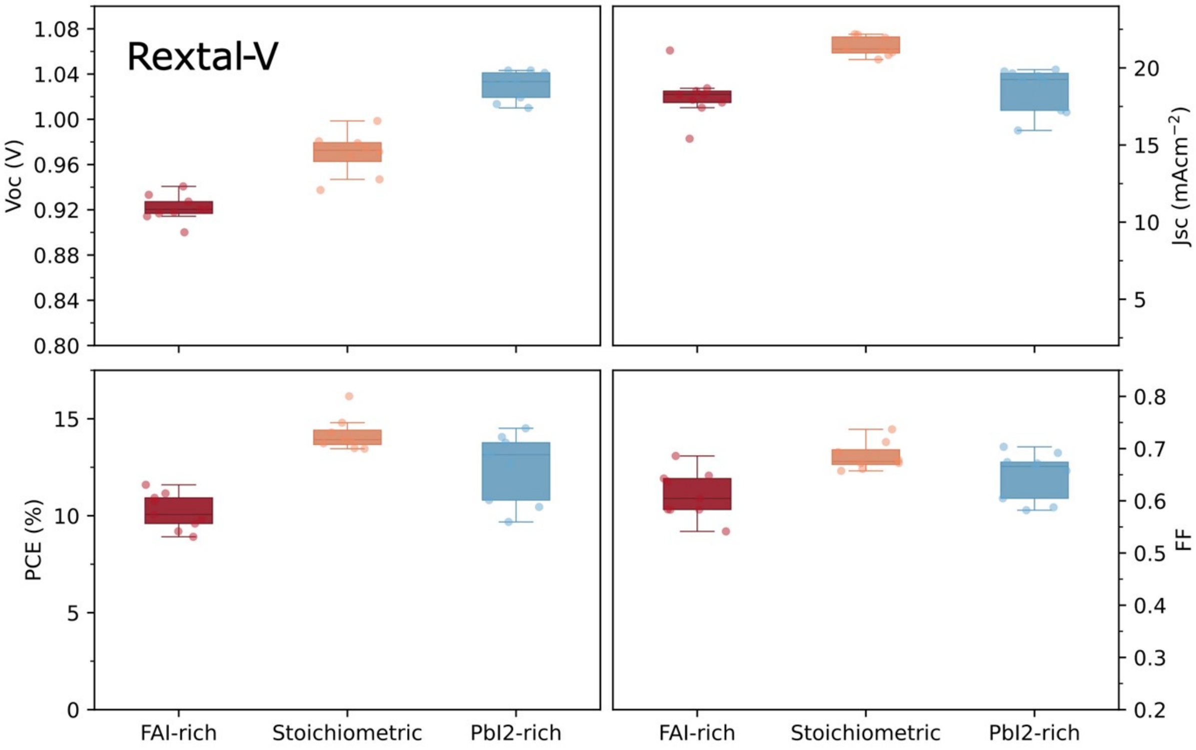

Figure S16 Stoichiometry optimisation for $FAPbI_3$ perovskite devices fabricated with recrystallised FAI (rextal-V). Device performance parameters are shown for FAI-rich (FAI +5 mol%), stoichiometric ($FAI:PbI_2 = 1:1$) and PbI_2-rich (PbI_2 +5 mol%) conditions. In the box plots, the central line inside each box represents the median value of the dataset. The box edges (lower and upper sides) indicate the first quartile (Q1) and third quartile (Q3), corresponding to the 25th and 75th percentiles, respectively. The whisker extends from the box to the smallest and largest data points within 1.5 times the interquartile range (IQR) from Q1 and Q3. Data points lying outside of this range are plotted individually as outliers.

Figures S15 and S16 show that for both ctrl-V and rextal-V devices, the maximum PCE is achieved at the nominal 1:1 $FAI:PbI_2$ ratio. Importantly, despite this optimisation, ctrl-V devices consistently exhibit significantly lower performance than rextal-V devices across all stoichiometries tested. This indicates that the reduced device performance observed for as-received FAI cannot be attributed solely to suboptimal stoichiometry, but is instead linked to differences in precursor quality.

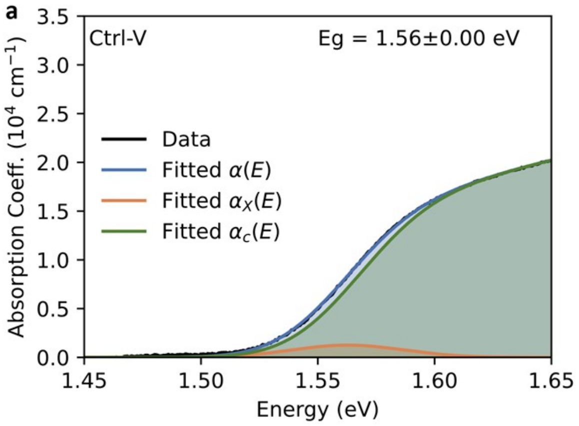

Figure S17 Elliott fitting results of the absorption coefficient values of vapour-deposited $FAPbI_3$ films fabricated using as-received and recrystallised FAI, labelled as ctrl-V and rextal-V, separately.

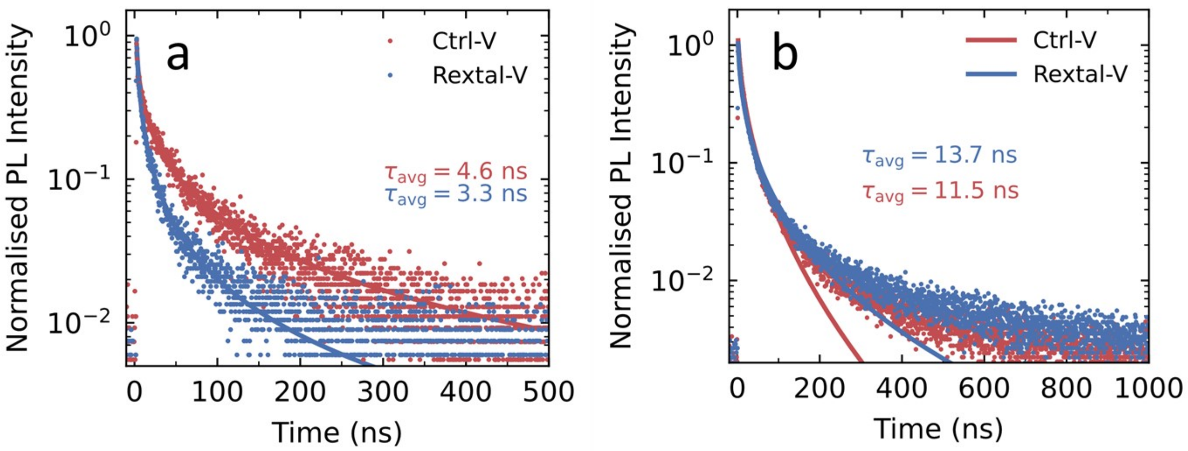

Figure S18 (a) PL dynamics of vapour-deposited $FAPbI_3$ films made using as-received FAI and recrystallised FAI, labelled as ctrl-V and rextal-V, separately, excited by 398nm laser, with the 1MHz repetition rate and the fluence of 45.4 nJ/cm^2. (b) PL dynamics of vapour-deposited $FAPbI_3$ films made using as-received FAI and recrystallised FAI, labelled as ctrl-V and rextal-V, respectively, excited by 510nm laser, with the 0.5MHz repetition rate and the fluence of 15.9 nJ/cm^2 per pulse. The lifetime is determined by fitting the data with a stretched exponential function. TRPL measurements in (a) and (b) yield similar charge-carrier dynamics in ctrl-V and rextal-V films, with a difference in lifetime of ~2 ns. We note here that in both cases, as is consistent with co-evaporated films of pure $FAPbI_3$,[7] the lifetimes of these films are very short, and as such, such small differences (or lack thereof) in the lifetime are not truly representative of any measurable changes in carrier dynamics.

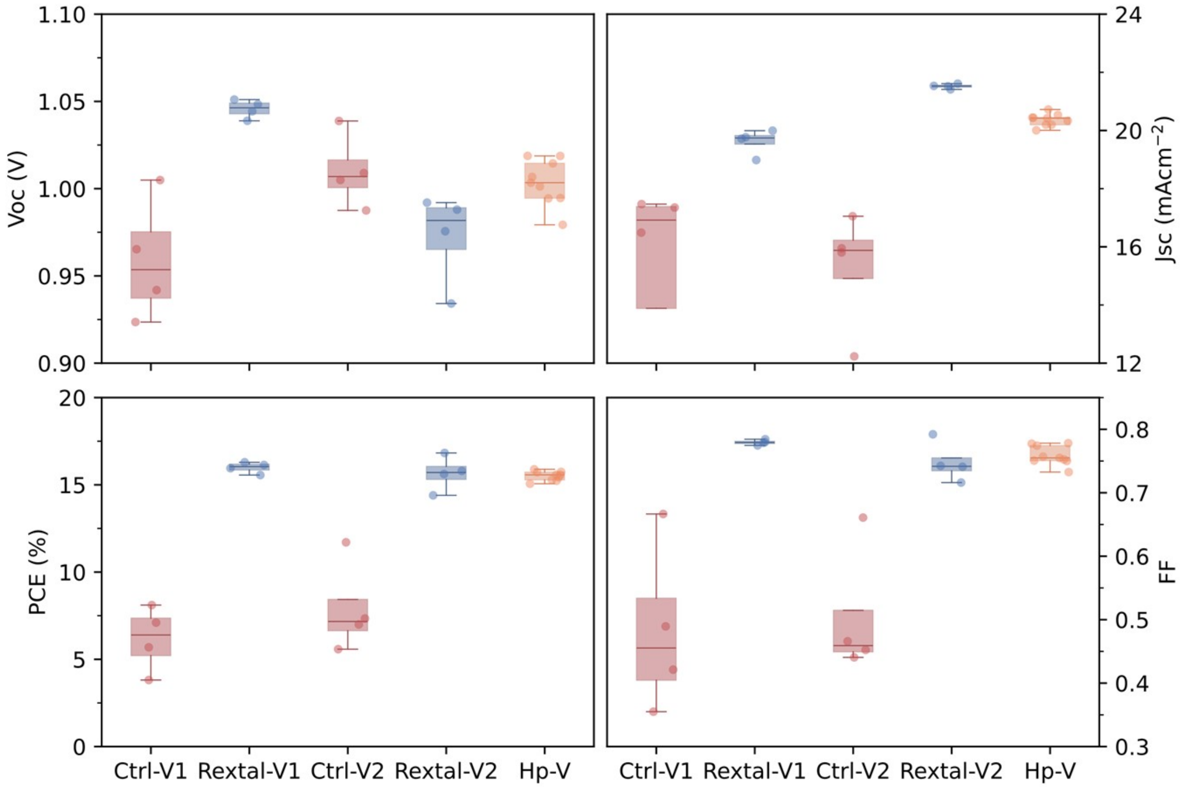

Figure S19 Statistical distribution of photovoltaic performance parameters of vapour-deposited $FAPbI_3$ MHP devices made by as-received and recrystallised FAI made in two separate batches (labelled as ctrl-V1, rextal-V1 and ctrl-V2, rextal-V2), as well as high-purity FAI (labelled as Hp-V).

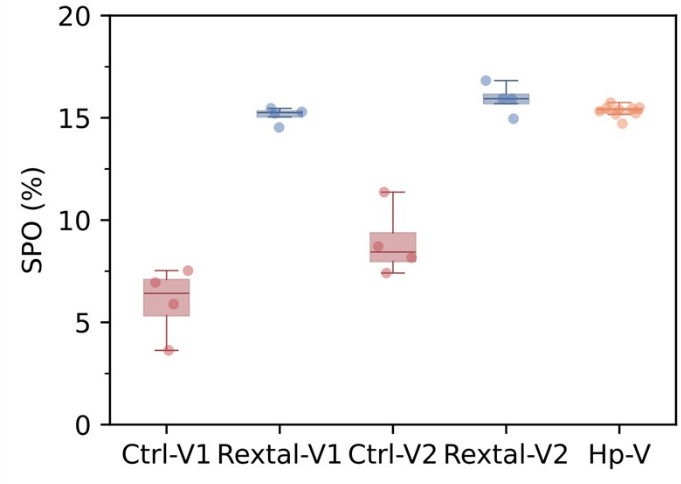

Figure S20 Stabilised power output of vapour-deposited $FAPbI_3$ MHP devices made by as-received and recrystallised FAI made in two separate batches (labelled as ctrl-V1, rextal-V1 and ctrl-V2, rextal-V2), as well as high-purity FAI (labelled as Hp-V).

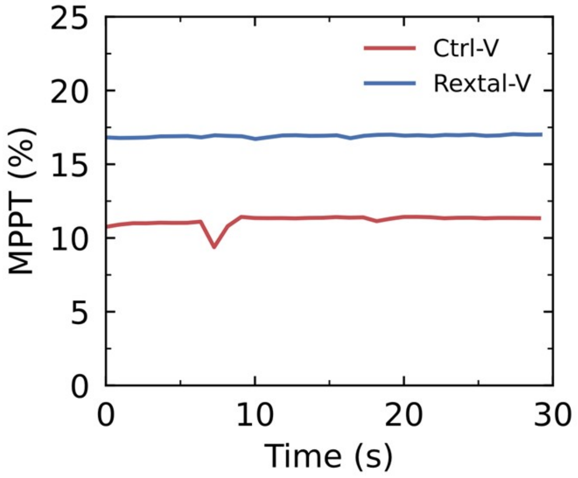

Figure S21 Maximum power output tracking (MPPT) of best vapour-deposited $FAPbI_3$ MHP devices made by as-received and recrystallised FAI (labelled as ctrl-Vand rextal-V).

Table S3 Comparison of photovoltaic performance of co-evaporated $FAPbI_3$ perovskite solar cells in this work with other literature. Please note that the devices listed here do not employ any passivation layers or additives.

Device structure	Perovskite composition	V_{oc} (V)	J_{sc} (mA cm^{-2})	FF (%)	PCE (%)	Refs
Glass/ITO/MeO-2PACz/MHP/C60/BCP/Cu	$FAPbI_3$	-	-	-	16	[6]
Glass/FTO/C60/MHP/spiro-OMeTAD/Ag	$FAPbI_3$	1.01	22.1		15.8	[7]
Glass/ITO/MeO-2PACz/MHP/C60/BCP/Cu	$FAPbI_3$	1.07	20.16	0.70	15.09	[8]
Glass/ITO/PTAA/MHP/C60/BCP/Cu	$FAPbI_3$	1.07	17.3	0.68	12.62	[8]
Glass/ITO/PTAA/MHP/C60/BCP/Ag	$FAPbI_3$ (as-received FAI)	1.04	17.05	0.66	11.71	This work
Glass/ITO/PTAA/MHP/C60/BCP/Ag	$FAPbI_3$ (recrystallised FAI)	0.99	21.41	0.79	16.83	This work

For comparison, we have compiled a list of the photovoltaic performance of a number of co-evaporated $FAPbI_3$ perovskite solar cells reported in the literature in Table SX1. When as-received FAI is employed, the resulting device performance is comparable to previously reported devices with similar p-i-n architectures (Glass/ITO/PTAA/MHP/C60/BCP/Ag or Cu). In our current case, when recrystallised FAI is used, our devices exhibit comparable and even slightly improved performance relative to reported devices employing n-i-p architectures or MeO-2PACz-based hole transport layers. Notably, within a standard p-i-n architecture using PTAA as an HTL and pure $FAPbI_3$ as the absorber layer, our co-evaporated devices achieve higher performance than previously reported values under similar conditions.

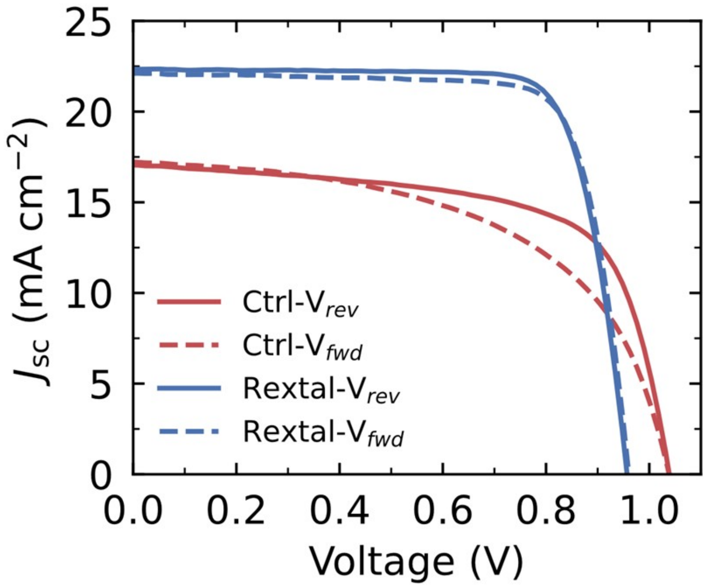

Figure S22 Current density-voltage curve of best vapour-deposited $FAPbI_3$ MHP devices made by as-received and recrystallised FAI, labelled as ctrl-V and rextal-V, separately.

Table S4 Champion and average device performance parameters for vapour-deposited $FAPbI_3$ perovskite solar cells fabricated with as-received (ctrl-V) and recrystallised (rextal-V) FAI measured under 1 sun simulated AM1.5G solar illumination. The values given in this table represent scans from open-circuit to short-circuit conditions.

Device		J_{sc} (mA cm^{-2})	V_{oc} (V)	PCE (%)	FF	SPO (%)
Ctrl-V	Champion	17.05	1.04	11.71	0.66	11.37
	Avg	14.20±5.18	0.92±0.16	6.16±2.77	0.49±0.12	6.00±1.72
Rextal-V	Champion	21.41	0.99	16.83	0.79	16.82
	Avg	20.90±1.11	0.99±0.04	15.63±0.92	0.76±0.03	15.12±0.41

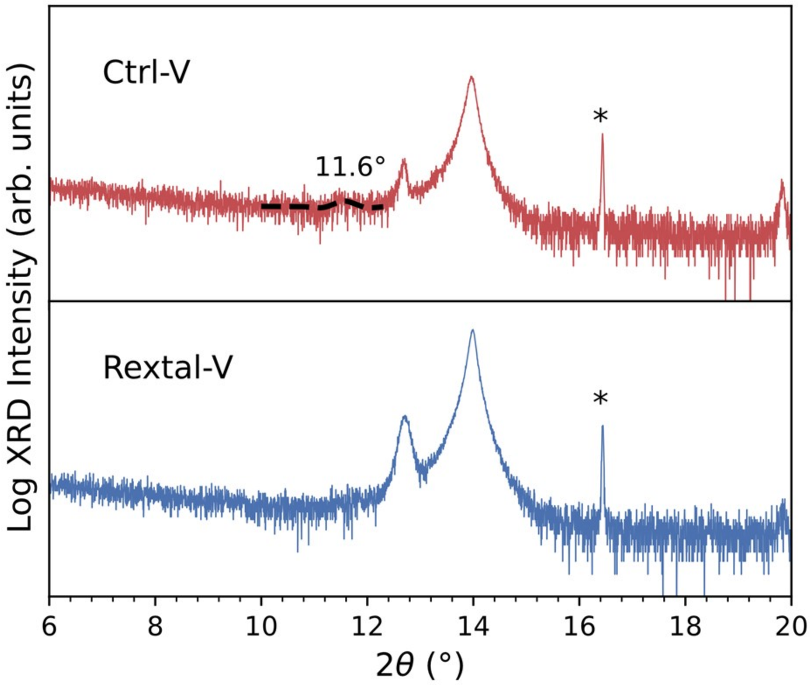

Figure S23 X-ray diffraction patterns of ctrl-V and rextal-V films from different batches. XRD signal from polytype is only identified in ctrl-V films. The asterisk (*) denotes the quartz reference peak at 16.44° used for peak position calibration.

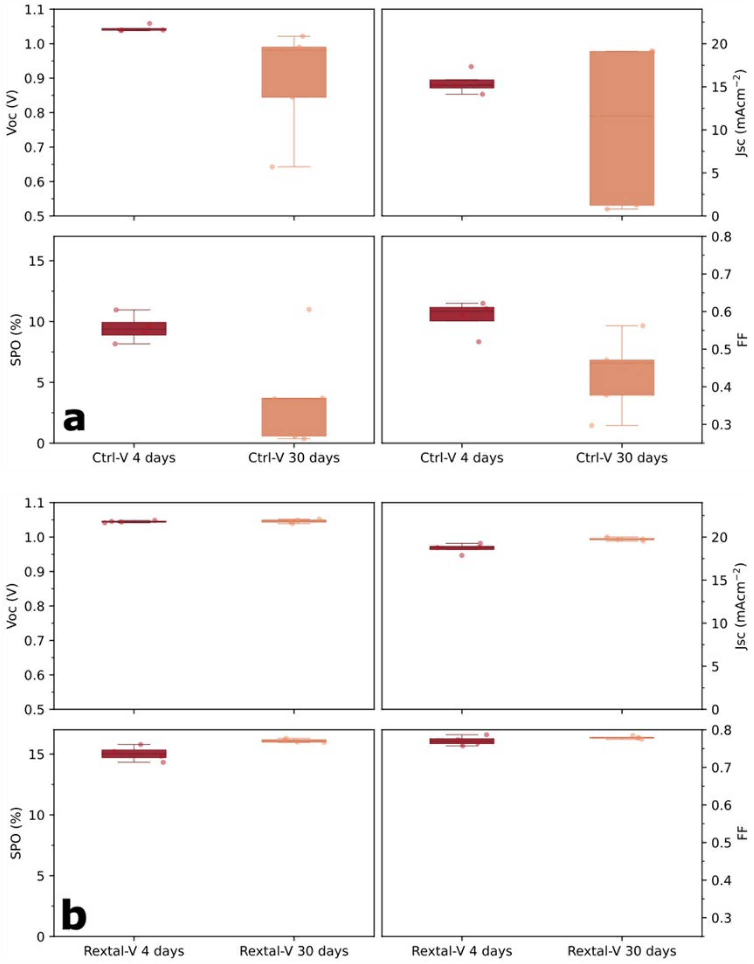

Figure S24 Performance parameters of $FAPbI_3$ perovskite devices fabricated with as-received (ctrl-V) and recrystallised FAI (rextal-V) after storage in the glovebox for 4 days (a) and 30 days (b). In the box plots, the central line inside each box represents the median value of the dataset. The box edges (lower and upper sides) indicate the first quartile (Q1) and third quartile (Q3), corresponding to the 25th and 75th percentiles, respectively. The whisker extends from the box to the smallest and largest data points within 1.5 times the interquartile range (IQR) from Q1 and Q3. Data points lying outside of this range are plotted individually as outliers.

4. Degradation Study of Vapour-Deposited FAI

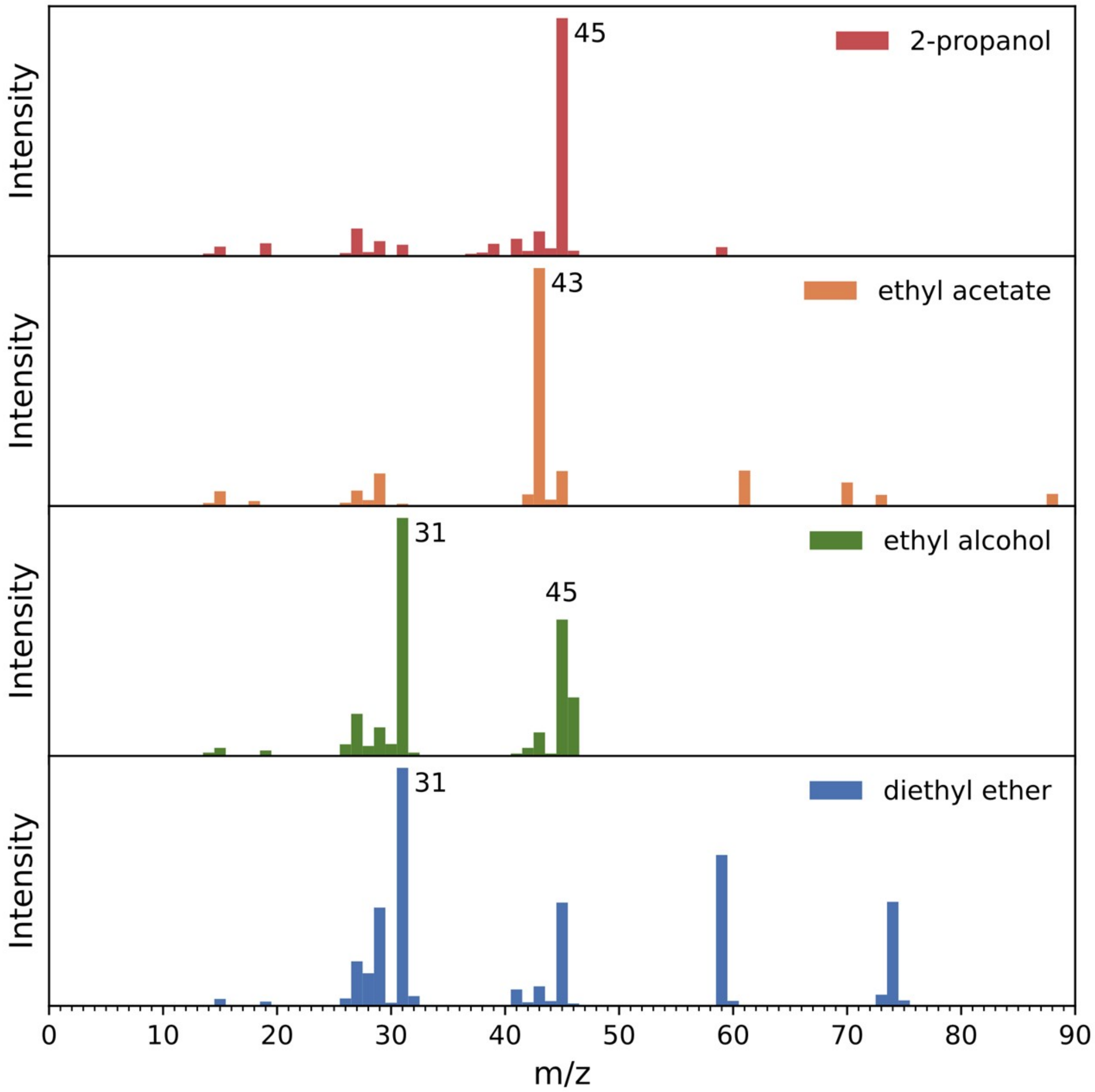

Figure S25 Reference mass spectroscopy patterns of impurities, including 2-propanol (isopropanol), ethyl acetate, ethyl alcohol (ethanol), diethyl ether.[9]

Table S5 List of m/z values of molecules detected in mass spectrometry measurements.

m/z	Detected ion	Likely parent/fragment molecule
14	N^+	nitrogen
16	NH_2^+	NH_3 fragment
17	NH_3^+	NH_3 parent peak
18	H_2O^+	H_2O parent peak
27	HCN^+/ CHN^+	HCN parent peak/FAI fragment
28	N_2^+	nitrogen
31	CH_2OH^+	major fragment of ethanol
43	CH_3CO^+	major fragment of ethyl acetate
45	CH_3CHOH^+	major fragment of isopropyl alcohol
54	$HCN(H)CN^+$	major fragment of sym-triazine
81	$C_3H_3N_3^+$	sym-triazine parent peak

Table S6 List of boiling/sublimation temperatures of materials at normal atmospheric pressure (1 atm). Sourced from NIST Standard Reference Database[10]

Materials	Boiling/Sublimation temperatures at normal atmospheric pressure (1 atm) (°C)
Ethyl Acetate (EtOAc)	77.1
Ethanol (EtOH)	78.4
Isopropanol (IPA)	82.6
Diethyl Ether	46.7
Formamidinium iodide (FAI) (sublimate/decompose)	~220

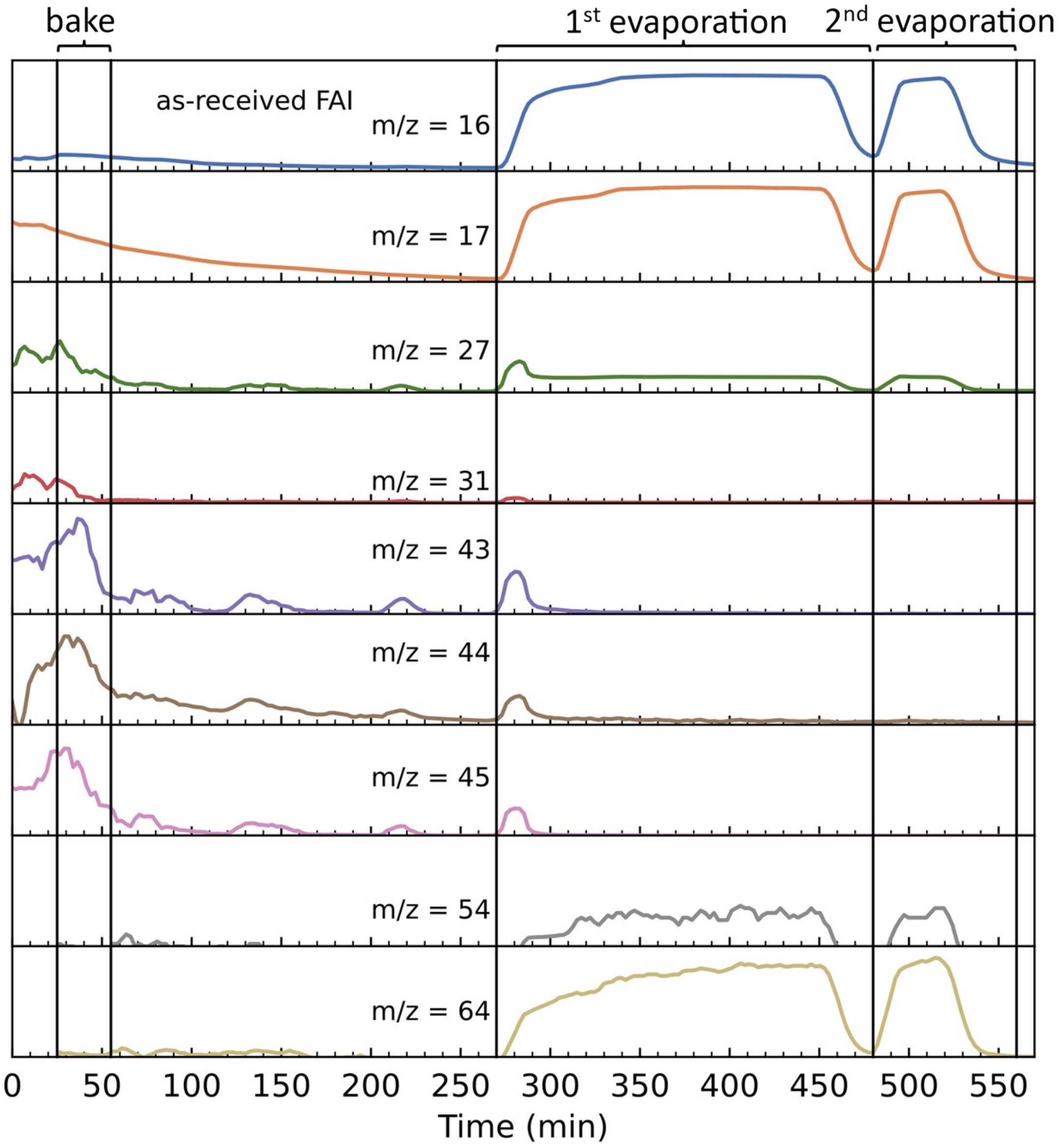

Figure S26 Mass spectra tracking of as-received FAI during low-temperature preheating (~130°C, 30 min), the 1st deposition (~177°C, 180 min), and the 2nd deposition (>180°C, 30 min) recorded with the Faraday detector of the residual gas analysis (RGA) system.

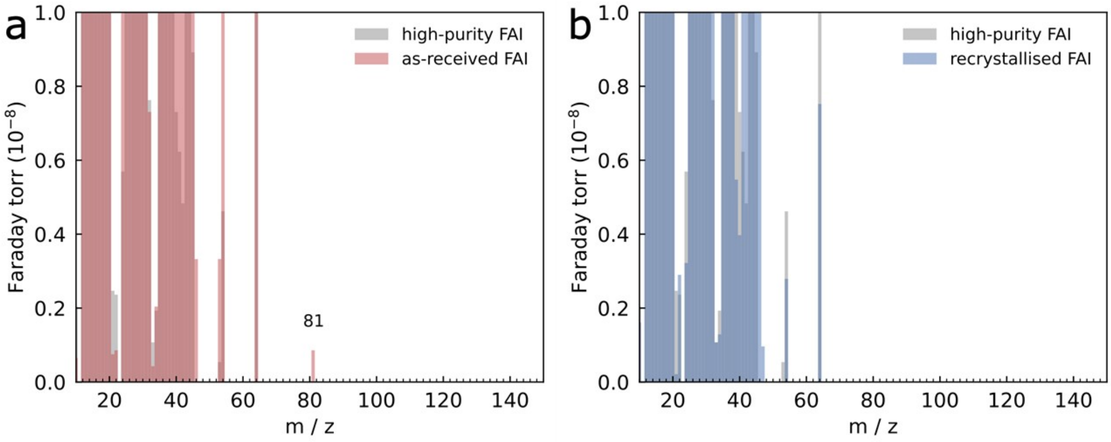

Figure S27 (a) Comparison of the cracking pattern of as-received FAI (red) and high-purity FAI (grey). (b) Comparison of the cracking pattern of recrystallised FAI (blue) and high-purity FAI (grey). The integration window for all cracking patterns shown in (a) and (b) is 20 cycles of the RGA scan, corresponding to an acquisition time of approximately 30 min. The cracking patterns shown here are the zoomed-in patterns shown in the main text (Figure 5c and 5d).

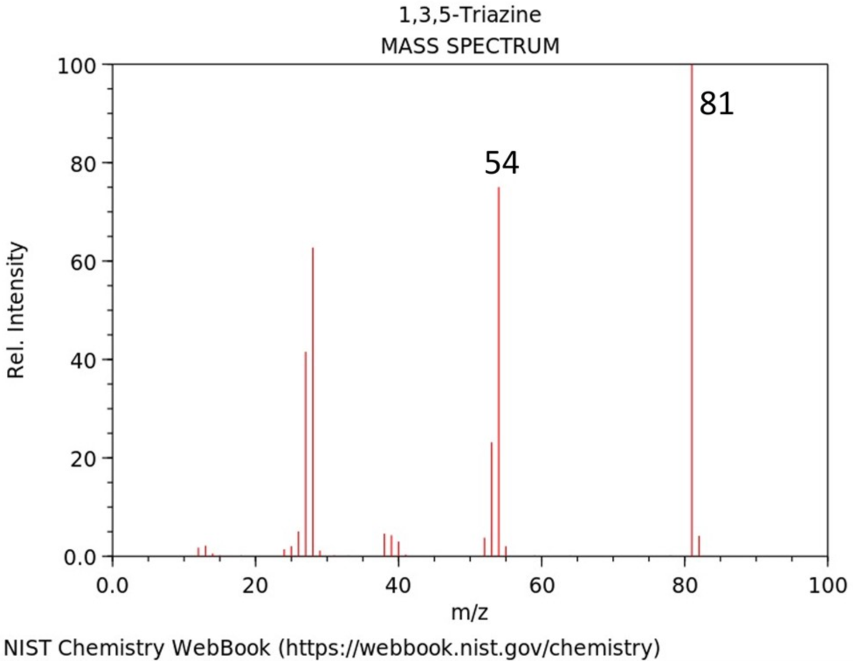

Figure S28 Fragmentation patterns m/z peaks retrieved from the NIST MS library data (http://webbook.nist.gov/chemistry/) for sym-triazine.

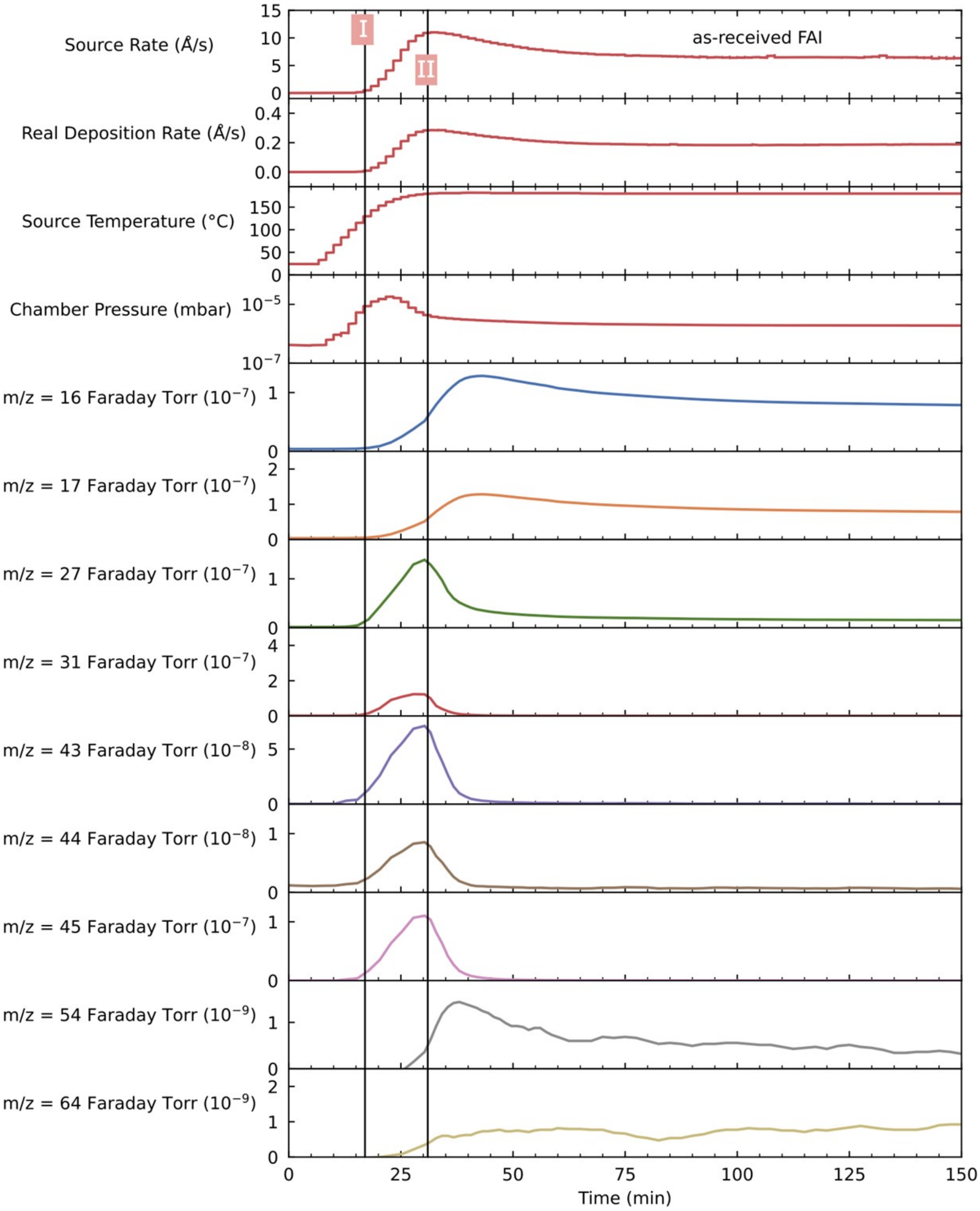

Figure S29 Evaporation parameters and mass spectra tracking of as-received FAI during the vapour deposition. Line I represents the time point at which both the source QCM and real deposition rates begin to increase, coinciding with the initial rise in the main MS signals of EtOH (m/z = 31), EtOAc (m/z = 43), and IPA (m/z = 45). Line II labels the time point at which both the source and substrate rates reach their maximum values, aligning with the peak intensities of the MS signals for EtOH (m/z = 31), EtOAc (m/z = 43), and IPA (m/z = 45). These results demonstrate that the evaporation of impurities (EtOH, EtOAc, and IPA) in as-received FAI can affect the readings of the source and substrate sensors.

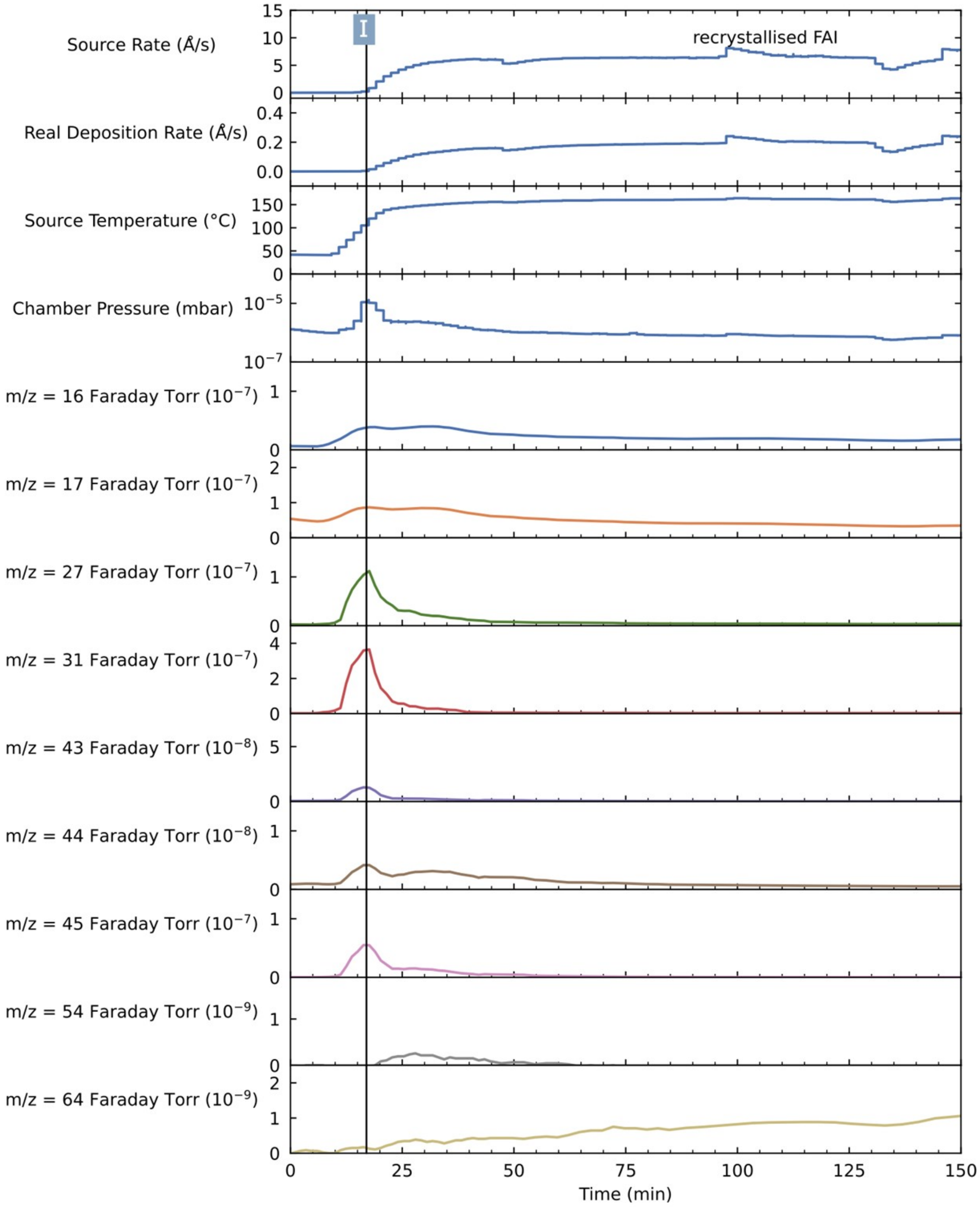

Figure S30 Evaporation parameters and mass spectra tracking of recrystallised FAI during the vapour deposition. Line I represents the time point at which both the source QCM and real deposition rates begin to increase, coinciding with the time point at which both the chamber pressure and the main MS signals of diethyl ether ($m/z = 31, 45$) reach their maximum values. This suggests that the evaporation of diethyl ether does not contribute to the increase of the source rate and substrate rate. Instead, it leads to a rise in chamber pressure, which is consistent with the high vapour pressure of diethyl ether resulting from its low boiling point (Table S6).

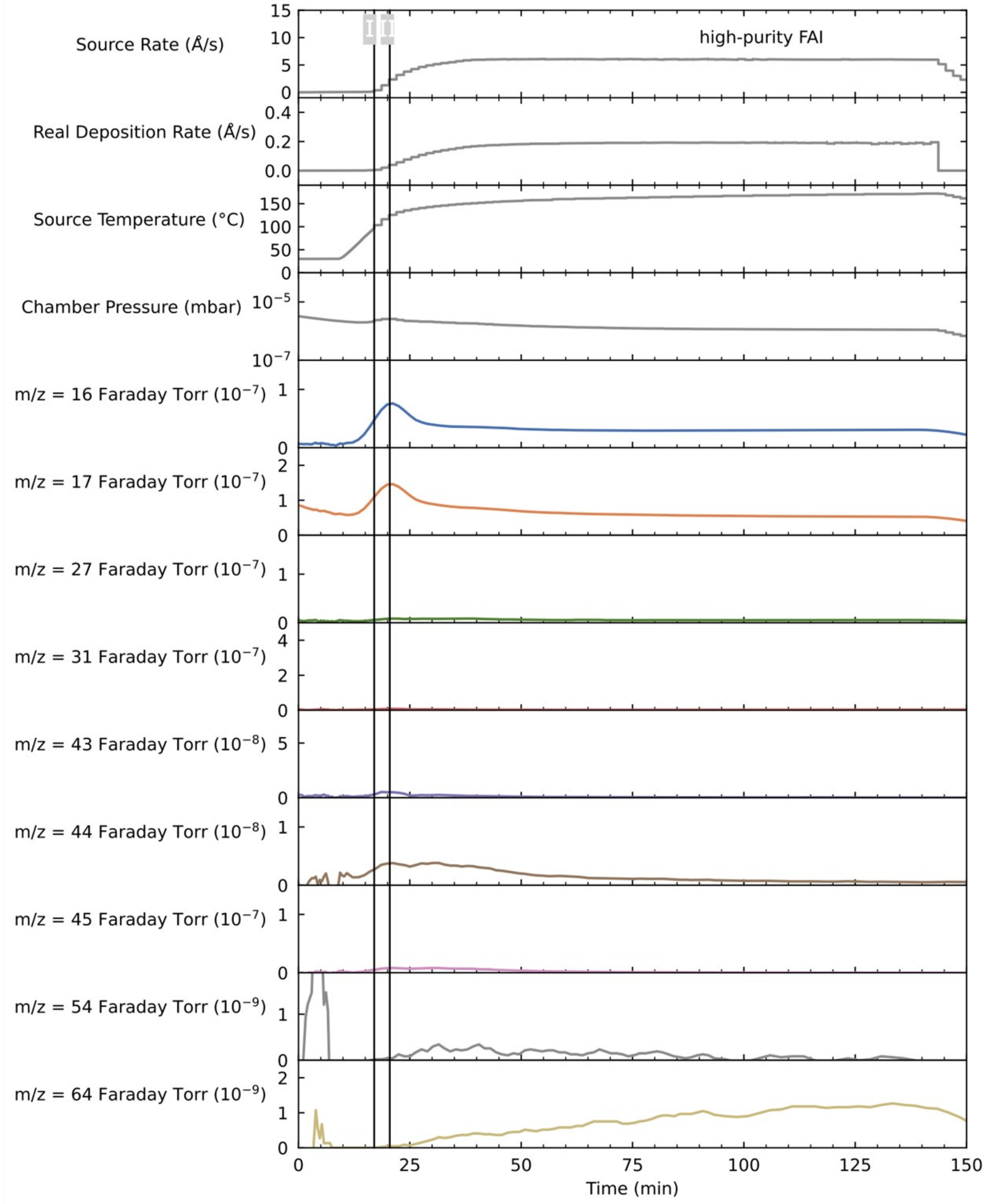

Figure S31 Evaporation parameters and mass spectra tracking of high-purity FAI during the vapour deposition. Line I represents the time point at which both the source QCM and real deposition rates begin to increase, coinciding with the initial rise in the main MS signals of FAI (m/z = 44). Line II labels the time point at which the chamber pressure reaches its maximum, aligning with the peak intensities of the MS signals for FAI (m/z = 44). These results suggest that for high-purity FAI, the evaporation of FAI primarily influences the sensor rates and the chamber pressure.

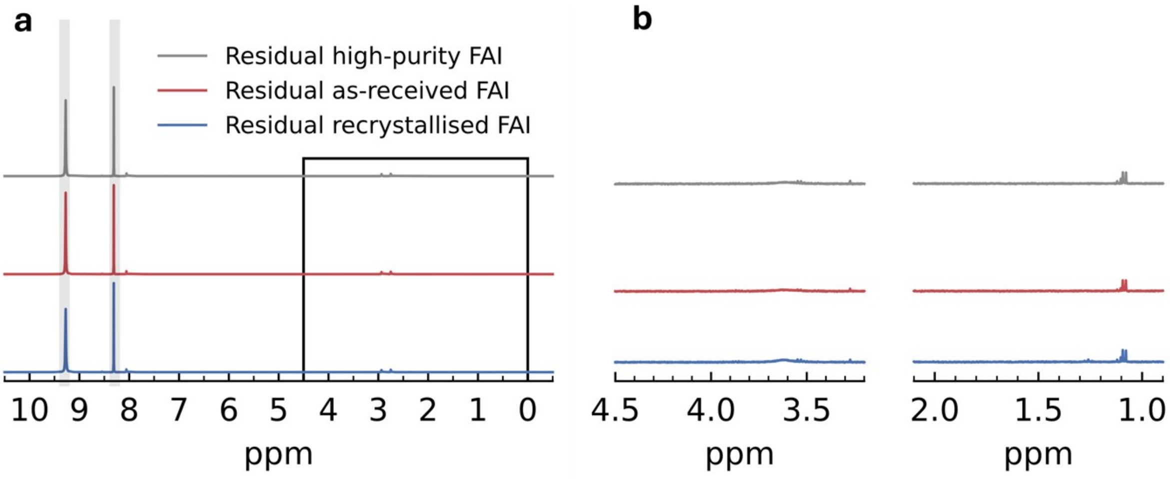

Figure S32 Liquid-state ^{1}H NMR characterisation results of residual high-purity FAI, recrystallised FAI and as-received FAI powder after evaporation (Figures S29-S31), dissolved in DMF-d_7. In as-received FAI, no signals are detected from either impurities (ethyl acetate, ethanol, and isopropanol) or degradation products (hydrogen cyanide, sym-triazine, and ammonia).

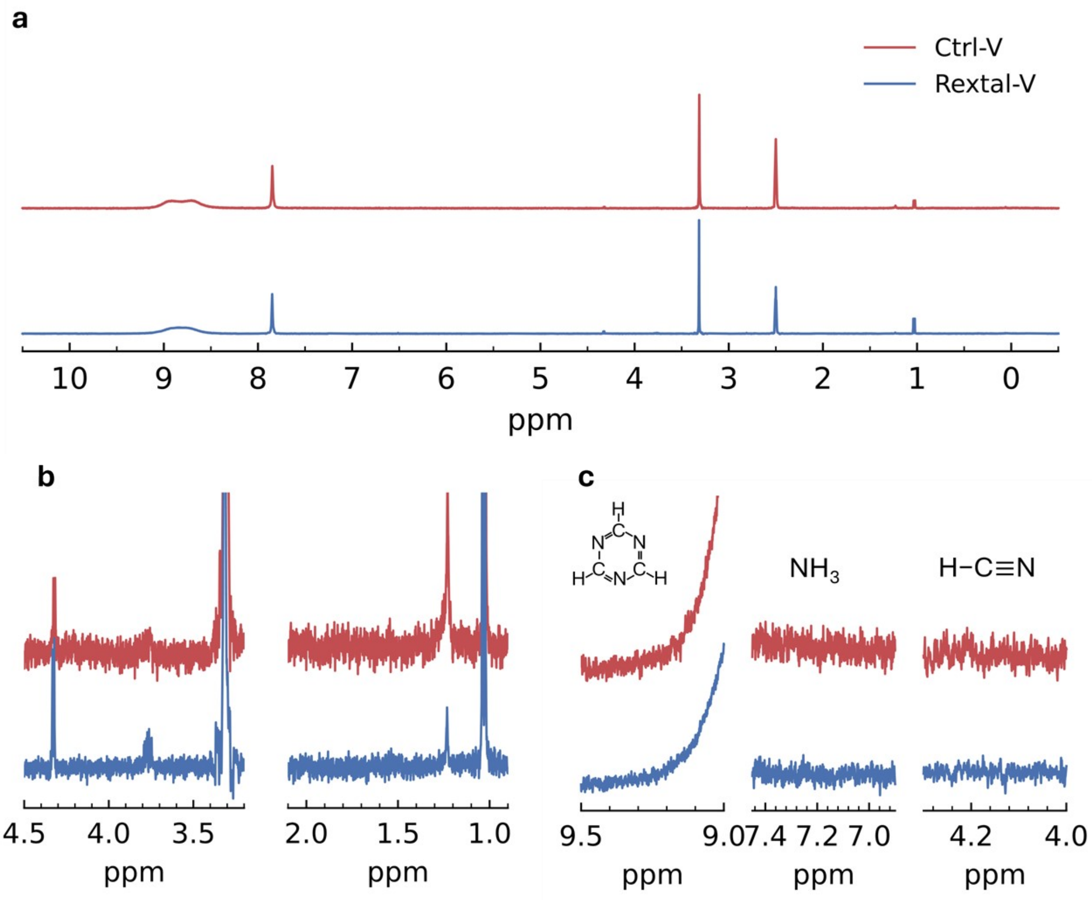

Figure S33 (a) Liquid-state ^{1}H NMR characterisation results of as-deposited vapour-deposited $FAPbI_3$ films fabricated using as-received (ctrl-V) and recrystallised (rextal-V) FAI redissolved in DMSO-d$_6$. Signals from FAI impurities (b) or degradation products (c) are not observed in both cases.

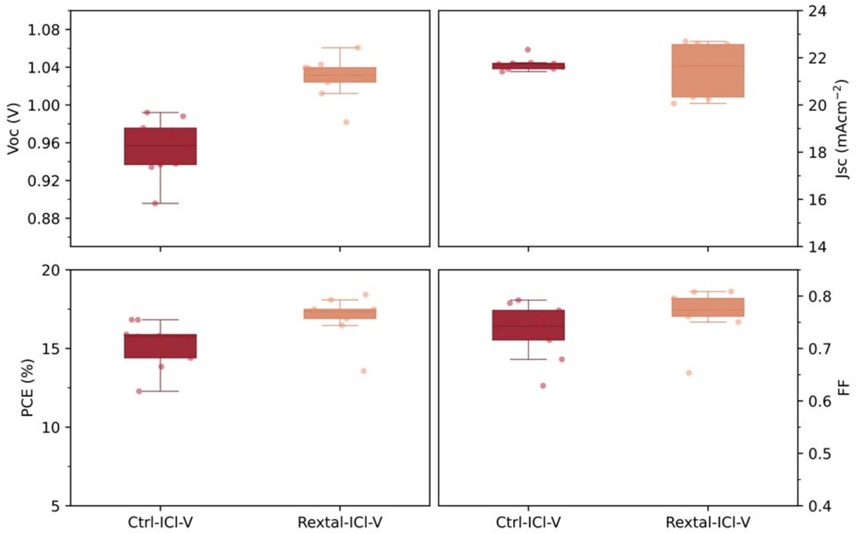

Figure S34 Performance parameters of co-evaporated $FA_{0.9}Cs_{0.1}Pb(I_{1-x}Cl_x)_3$ perovskite devices fabricated with as-received (ctrl-V) and recrystallised FAI (rextal-V). In the box plots, the central line inside each box represents the median value of the dataset. The box edges (lower and upper sides) indicate the first quartile (Q1) and third quartile (Q3), corresponding to the 25th and 75th percentiles, respectively. The whisker extends from the box to the smallest and largest data points within 1.5 times the interquartile range (IQR) from Q1 and Q3. Data points lying outside of this range are plotted individually as outliers.

We observe that incorporating additional components (e.g., CsI and $PbCl_2$) can partially improve the performance of devices fabricated using as-received FAI (Figure R8). However, even under these conditions, rextal-V devices consistently outperform ctrl-V devices. These results demonstrate that while process optimisation can influence device performance, precursor purification provides a more robust and reproducible pathway to achieving high-performance vapour-deposited perovskite devices.

References

1. K. A. Elmestekawy, A. D. Wright, K. B. Lohmann, J. Borchert, M. B. Johnston and L. M. Herz, *ACS Nano*, 2022, **16**, 9640–9650.

2. C. L. Davies, M. R. Filip, J. B. Patel, T. W. Crothers, C. Verdi, A. D. Wright, R. L. Milot, F. Giustino, M. B. Johnston and L. M. Herz, *Nat. Commun*., 2018, **9**, 293.

3. K. Tanaka, T. Takahashi, T. Ban, T. Kondo, K. Uchida and N. Miura, *Solid State Commun*., 2003, **127**, 619–623.

4. A. D. Wright, C. Verdi, R. L. Milot, G. E. Eperon, M. A. Pérez-Osorio, H. J. Snaith, F. Giustino, M. B. Johnston and L. M. Herz, *Nat. Commun*., 2016, **7**, 11755.

5. R. D. J. Oliver, P. Caprioglio, F. Peña-Camargo, L. R. V. Buizza, F. Zu, A. J. Ramadan, S. G. Motti, S. Mahesh, M. M. McCarthy, J. H. Warby, Y.-H. Lin, N. Koch, S. Albrecht, L. M. Herz, M. B. Johnston, D. Neher, M. Stolterfoht and H. J. Snaith, *Energy Environ. Sci*., 2022, **15**, 714–726.

6. M. Roß, S. Severin, M. B. Stutz, P. Wagner, H. Köbler, M. Favin-Lévêque, A. Al-Ashouri, P. Korb, P. Tockhorn, A. Abate, B. Stannowski, B. Rech and S. Albrecht, *Adv. Energy Mater*., 2021, **11**, 2101460.

7. J. Borchert, R. L. Milot, J. B. Patel, C. L. Davies, A. D. Wright, L. Martínez Maestro, H. J. Snaith, L. M. Herz and M. B. Johnston, *ACS Energy Lett*., 2017, **2**, 2799–2804.

8. T. C.-J. Yang, T. Kang, M. Fitzsimmons, G. Vega, Y. Lu, L. Rosado, A. Jiménez-Solano, L. Pan, S. J. Zelewski, J. Ferrer Orri, Y.-H. Chiang, D. Guo, Z. Y. Ooi, Y. Han, W. Xu, B. Roose, C. Ducati, S. Carretero Palacios, M. Anaya and S. D. Stranks, *EES Solar*, 2025, **1**, 41–55.

9. National Institute of Advanced Industrial Science and Technology (AIST), Spectral Database for Organic Compounds (SDBS), AIST, Tsukuba, Japan, 2025, https://sdbs.db.aist.go.jp/.

10. P. J. Linstrom and W. G. Mallard, NIST Chemistry WebBook, NIST Standard Reference Database No. 69, National Institute of Standards and Technology, Gaithersburg, MD, USA, https://doi.org/10.18434/T4D303.